Juncture Flow Computations using kL-Based Turbulence Models (Invited Paper)

K. S. Abdol-Hamid*, Nash'at N. Ahmad†, Jan-Renee Carlson‡, Robert T. Biedron§
NASA Langley Research Center, Hampton, Virginia, 23681

The development and implementation of kL-based Reynolds-Average Navier-Stokes (RANS) two-equation turbulence models are reported in this paper. The kL model is based on Abdol-Hamid's closure and Menter's modification to Rotta's two-equation model. Rotta showed that a reliable transport equation can be formed from the turbulence length scale *L*, and the turbulence kinetic energy *k*. Rotta's kL equation is well suited for a term-by-term modeling and displays useful features compared to other scale formulations. One of the important differences is the inclusion of higher-order velocity derivatives in the source terms of the scale equation. This can enhance the ability of RANS solvers to simulate unsteady flows in URANS mode. The k-kL scheme has been modified to include the Algebraic Reynolds Stress Model (ARSM) and the Quadratic Constitutive Relation (QCR) as nonlinear models. These models have gone through extensive validations using two-dimensional benchmark problems. The present study documents the application of the k-kL schemes to simulate flow around the Juncture Flow Model (JFM). The k-kL prediction results show generally good comparisons with measurements. The results from this formulation are similar to, or better than results using the SA-RC-QCR2000 two-equation turbulence model. The ARSM and the QCR formulations of k-kL show promise with a similar level of computational resources as basic two-equation turbulence models.

I. Introduction

Work on the Juncture Flow (JF) Experiment[1-3] effort was initiated by the National Aeronautics and Space Administration in 2014. The main objective of this project is to accurately measure the detailed flow field in the wing-fuselage juncture area, in order to assess the performance of the currently implemented turbulence models, and to advance the state-of-the-art in turbulence modeling based on JF measurements. Computational Fluid Dynamics (CFD) models in the past have had difficulty predicting the flow separation in the wing-fuselage juncture region.[4-6] Solutions from different codes and turbulence schemes have shown large variations in the prediction of separation initiation location, and in the size and shape of the separation bubble.

A series of risk-reduction wind tunnel tests[7-9] accompanied with CFD analyses[10] were conducted to select the wing-body geometry, test configuration, and the reference conditions. Additional tests and simulations were done to quantify the tunnel boundary conditions.[11-12] The first set of juncture flow experiments were conducted in NASA Langley's 14- by 22-foot subsonic wind tunnel (14x22) from November 2017 to March 2018. The result is an exceptionally detailed and well documented CFD validation-quality data set,[13-14] which is publicly available from NASA's Turbulence Modeling Resource (TMR) website.[15] An assessment of NASA's FUN3D[16] and OVERFLOW[17] codes based on comparison with the JF data is given in Rumsey et al.[18] and Lee and Pulliam,[19] respectively.

The purpose of this study was to evaluate the k-kL family of turbulence schemes developed by Abdol-Hamid[20-27] using the JF measurements. In the following sections, an overview of the Juncture Flow Experiment is given. The turbulence models used in the study are described in detail, and the results of the model evaluation using the wind tunnel data are discussed. Preliminary results of the in-tunnel simulations using FUN3D's overset[28] and wind tunnel controller[29] capabilities are also presented.

---

* Research Scientist, Configuration Aerodynamics Branch. Associate Fellow, AIAA.
† Research Scientist, Computational Aerosciences Branch. Senior Member, AIAA.
‡ Research Scientist, Computational Aerosciences Branch. Associate Fellow, AIAA.
§ Research Scientist, Computational Aerosciences Branch.

II. Juncture Flow Experiment

The first set of Juncture Flow experiments were conducted in NASA Langley's 14x22 wind tunnel from November 2017 to March 2018. The details of these tests are given in Kegerise and Neuhart[13] and in Kegerise et al.[14] The JF model was mounted on a sting-mast assembly that could vary the pitch and roll angles. The data were collected for $\alpha \in \left[-10°, 10°\right]$ with increments of 2.5°. The flow was tripped near the nose and on the upper and lower surfaces of the wing to ensure transition to a fully turbulent boundary layer. Figure 1 shows the JF model in the 14x22 wind tunnel.

A Laser Doppler Velocimetry (LDV) system was built for the experiment and placed inside the fuselage to measure the flow field in the juncture region. The sides of the fuselage were designed to be flat for easier access to the LDV system installed inside the fuselage and for more precise data collection. The LDV measured the profiles of mean velocity components, and turbulence quantities (shear and normal stresses, as well as all components of the velocity triple products) in the juncture region. The LDV data were also collected at other select locations on the wing and the fuselage. Around 30,000 samples were taken at each measurement location by the LDV probes. In addition to the LDV, a two-dimensional Particle Image Velocimetry (PIV) system was designed to measure the velocity flow fields at selected locations.[30] Although not as detailed as the LDV, the PIV provided a global view of the flow characteristics and a means to cross check the LDV measurements.

The transition locations on the JF model were verified with the help of infrared imaging. Oil flow visualization was used to provide an estimate of the separation bubble size. The oil flow visualization also gave qualitative insights into the separation bubble structure. A large number of static pressure ports were installed on the model wing (266) and on the fuselage (247). Static pressure data were also collected on the tunnel walls. In addition, unsteady pressure data were collected in the junction flow area of the starboard wing. The experiment also collected data on aeroelastic deflections of the wing.

A substantial effort was made to precisely quantify the model geometry, and the tunnel reference and boundary conditions. The resulting high-quality benchmark data set is unprecedented in detail and will be invaluable in not only the validation of existing turbulence models but also in the development of new, more advanced models.

Figure 1. The Juncture Flow Model in the NASA Langley Research Center's 14- by 22-Foot Subsonic Tunnel.

Although the main focus of the JF experiment is to collect CFD-validation quality measurements, the data can also be valuable in understanding the underlying physics that governs juncture flows, which are currently not well understood. Gand et al.[31] and Simpson[32] have provided detailed reviews on the topic. Previous research has shown that several factors influence the flow separation in the junction region. The horseshoe vortex generated at the leading edge of the wing due to the roll up of the boundary layer is considered as one of the contributing factors.[31] The strength and location of the horseshoe vortex have been linked with the shape of the wing's leading edge. The vorticity-induced perturbations in the wing boundary layer interact with the fuselage boundary layer in the juncture region, which can cause flow separation. The wing shape and orientation play a role in the formation of the separation bubble, and on the size and shape of the bubble (see Refs. 2 and 8). Other factors such as "the Reynolds number, displacement thickness of the approach boundary layer, the free-stream turbulence level, the roughness of the surfaces" [32] also affect the formation of juncture flows.

III. Fully Unstructured Navier-Stokes 3D (FUN3D) Code

The Fully Unstructured Navier-Stokes 3D (FUN3D) is a versatile code that has been used to solve complex flow problems ranging from hypersonics to aeroacoustics (`https://fun3d.larc.nasa.gov`).[33-34] FUN3D is based on a node-centered, finite-volume scheme designed to compute both compressible and incompressible flows on grids with different types of elements (tetrahedron, pyramid, prism, and hexahedron elements). FUN3D uses an artificial compressibility method for incompressible flows (Anderson et al.).[35] Several schemes are available for computing the convective fluxes. Computation of viscous fluxes on tetrahedral meshes is based on the Green-Gauss theorem and on nontetrahedral grids, an edge-derivative augmentation is employed to avoid odd-even decoupling. A number of turbulence models (`https://turbmodels.larc.nasa.gov`)[15] have been implemented in the code that range from single equation models to hybrid Reynolds-Averaged Navier-Stokes/Large Eddy Simulation (RANS/LES) capability. Time integration is based on a backward-Euler scheme with local time-stepping to accelerate convergence.[36]

IV. Turbulence Models

Abdol-Hamid's k-kL models[25-27] and the Spalart-Allmaras (SA)[37] model with the rotation-curvature (RC)[38] correction, and the quadratic constitutive relation (QCR)[39] are described in this section. The baseline k-kL scheme is also referred to in the literature as k-kL-MEAH2015, where 'MEAH' stands for Menter-Egorov-Abdol-Hamid. For brevity, k-kL-MEAH2015 is denoted by k-kL in this paper.

A. Baseline Linear k-kL Model

Abdol-Hamid's two-equation k-kL model is based on Rotta's approach[40] with the modifications proposed by Menter and Egorov.[41-42]

$$\frac{\partial \rho k}{\partial t}+\frac{\partial \rho u_j k}{\partial x_j}=P_k+\frac{\partial}{\partial x_j}\left(\left(\mu_l+\sigma_k\mu_t\right)\frac{\partial \rho k}{\partial x_j}\right)-C_w\mu_l\frac{k}{d^2}-C_k\rho\frac{k^{5/2}}{kL}, \tag{1}$$

$$\frac{\partial \rho kL}{\partial t}+\frac{\partial \rho u_j kL}{\partial x_j}=C_{(kL)1}\frac{kL}{k}P_{kL}+\frac{\partial}{\partial x_j}\left(\left(\mu_l+\sigma_{(kL)}\mu_t\right)\frac{\partial \rho kL}{\partial x_j}\right)-6\mu_l\frac{kL}{d^2}f_{(kL)}-C_{(kL)2}\rho k^{3/2}. \tag{2}$$

In Eqs. (1)-(2), ρ is the fluid density, k is the turbulence kinetic energy, u_i are the velocity components, P_k is the production of turbulence kinetic energy, P_{kL} is the production of turbulent kL, L is the turbulence length scale, μ_l is the bulk viscosity and μ_t is the turbulent viscosity. σ_k and $\sigma_{(kL)}$ are the diffusion coefficients. C_w, C_k, $C_{(kL)1}$, and $C_{(kL)2}$ are closure constants. $f_{(kL)}$ is an auxiliary function used in the kL transport equation, and d is the distance normal to the wall. The closure constants and functions are defined later in this section.

The linear k-kL approach assumes that the stress is directly proportional to strain:

$$\tau_{ij}=\tau_{ij}^{(k-kL)}=2\mu_t\left(S_{ij}-\frac{1}{3}tr\left\{S\right\}\delta_{ij}\right)-\frac{2}{3}\rho k\delta_{ij}, \tag{3}$$

where $S_{ij}=\frac{1}{2}\left(\frac{\partial u_i}{\partial x_j}+\frac{\partial u_j}{\partial x_i}\right)$ is the symmetric strain tensor.

The production terms, P_k and P_{kL} are given by

$$P_{kL}=P_k=\min\left(P,20C_\mu^{3/4}\frac{\rho k^{5/2}}{kL}\right), \tag{4}$$

where, $P = \mu_t S^2 = 2\mu_t S_{ij} S_{ij}$.

The turbulent eddy viscosity is computed as follows:

$$\mu_t = \frac{C_\mu^*}{C_\mu} C_\mu^{1/4} \frac{\rho(kL)}{k^{1/2}} = \frac{C_\mu^*}{C_\mu} \rho k \tau_t , \tag{5}$$

where, $\tau_t = C_\mu^{1/4} \dfrac{(kL)}{k^{3/2}}$ is the turbulent time scale.

In the linear approach, $C_\mu^* = C_\mu$. The closure functions and coefficients are defined as follows,

$$C_k = C_\mu^{3/4}, \quad C_{(kL)1} = \zeta_1 - \zeta_2 A_L^2, \quad A_L = \left(\frac{L}{L_{vk}}\right), \quad C_{(kL)2} = \zeta_3 ,$$

$$f_{(kL)} = \frac{1 + C_{d1}\xi}{1 + \xi^4}, \quad \xi = \frac{\rho\sqrt{0.3kd}}{20\mu_l} ,$$

$$L_{vk} = \kappa \left|\frac{U'}{U''}\right|, \quad U' = \sqrt{2S_{ij}S_{ij}} ,$$

where, κ is the von Kármán constant, and the second derivative of the velocity can be written as follows:

$$U'' = \sqrt{\frac{\partial^2 u_i}{\partial x_k^2}\frac{\partial^2 u_i}{\partial x_j^2}} = \sqrt{\left(\frac{\partial^2 u}{\partial x^2} + \frac{\partial^2 u}{\partial y^2} + \frac{\partial^2 u}{\partial z^2}\right)^2 + \left(\frac{\partial^2 v}{\partial x^2} + \frac{\partial^2 v}{\partial y^2} + \frac{\partial^2 v}{\partial z^2}\right)^2 + \left(\frac{\partial^2 w}{\partial x^2} + \frac{\partial^2 w}{\partial y^2} + \frac{\partial^2 w}{\partial z^2}\right)^2} . \tag{6}$$

Since, L_{vk} becomes singular as U' and U'' approach zero, the following limiters are defined

$$if\ \left(U'' = 0\ \ or\ \ U' = 0\right), \quad P_{kL} = 0 . \tag{7}$$

For all other conditions, following Menter et al.[41-42] with corrections for separated flows by Abdol-Hamid,[21] the following limit is applied on L_{vk}

$$if\ \left(U'' > 0\ \ and\ \ U' \geq 0\right),$$

$$L_{vk,\min} \leq L_{vk} \leq L_{vk,\max}, \quad L_{vk,\min} = \frac{kL}{kC_{11}}, \quad L_{vk,\max} = C_{12}\kappa d f_p ,$$

$$f_p = \min\left[\max\left(\frac{P_k kL}{C^{3/4}\rho k^{5/2}}, C_{13}\right), 1.0\right]. \tag{8}$$

The wall and farfield boundary conditions for k and kL for most applications are

$$k_{wall} = \left(kL\right)_{wall} = 0, \quad k_{\infty} = 9\times10^{-9}a_{\infty}^{2}, \quad \left(kL\right)_{\infty} = 1.5589\times10^{-6}\,\frac{\mu_{\infty}a_{\infty}}{\rho_{\infty}}, \tag{9}$$

where a_{∞}, μ_{∞}, ρ_{∞} are the reference speed of sound, viscosity, and density respectively. The constants are:

$$\sigma_{k} = 1.0, \quad \sigma_{(kL)} = 1.0\,.$$

$$\kappa = 0.41, \quad C_{\mu} = 0.09\,.$$

$$\zeta_{1} = 1.2, \quad \zeta_{2} = 0.97, \quad \zeta_{3} = 0.13\,.$$

$$C_{11} = 10.0, \quad C_{12} = 1.3, \quad C_{13} = 0.5, \quad C_{d1} = 4.7, \quad C_{w} = 2.0\,.$$

B. k-kL-ARSM Model

The k-kL-ARSM model is based on Rumsey and Gatski.[43-44] Nonlinearity in the model is added by defining the stress tensor as follows

$$\tau_{ij}^{(k-kL-ARSM)} = -\rho k\left(\beta_{1}T^{(1)} + \beta_{2}T^{(2)} + \beta_{4}T^{(4)} + \frac{2}{3}\delta_{ij}\right), \tag{10}$$

where, $T^{(1)}$, $T^{(2)}$, and $T^{(4)}$ are tensor polynomials which are functions of strain and vorticity rates given by

$$T^{(1)} = \left[S^{*} - \frac{1}{3}tr\left\{S^{*}\right\}\right], \quad T^{(2)} = \left[S^{*2} - \frac{1}{3}tr\left\{S^{*2}\right\}\right], \quad T^{(4)} = \left[S^{*}W^{*} - W^{*}S^{*}\right].$$

S_{ij} is the strain, and W_{ij} is the vorticity,

$$S_{ij} = \frac{1}{2}\left(\frac{\partial u_{i}}{\partial x_{j}} + \frac{\partial u_{j}}{\partial x_{i}}\right), \quad W_{ij} = \frac{1}{2}\left(\frac{\partial u_{i}}{\partial x_{j}} - \frac{\partial u_{j}}{\partial x_{i}}\right),$$

where, $W_{ij}^{*} = \tau W_{ij}$, $S_{ij}^{*} = \tau S_{ij}$, and τ is a constant defined later in this section.

$T^{(1)}$ is the linear part of the model, and $T^{(2)}$, and $T^{(4)}$ are the nonlinear terms that model anisotropy. The coefficients for these terms are given by

$$\beta_{1} = -2C_{\mu}^{*} = 2\alpha, \quad \beta_{2} = -2a_{4}a_{3}\beta_{1}, \quad \beta_{4} = a_{4}a_{2}\beta_{1}\,. \tag{11}$$

C_{μ}^{*} in Eq. (11) is limited to be no smaller than 0.0005.

For the cubic-based ARSM, α is the root of the cubic equation,

$$\alpha^{3} + p\alpha^{2} + q\alpha + r = 0\,. \tag{12}$$

The coefficients a_{1}, a_{2}, a_{3}, and a_{4} are given by

$$a_1 = \frac{1}{2}\left(\frac{4}{3} - C_2\right), \quad a_2 = \frac{1}{2}\left(2 - C_4\right), \quad a_3 = \frac{1}{2}\left(2 - C_3\right), \quad a_4 = \left[\gamma_1^* - 2\alpha\gamma_0^*\eta^2\right]^{-1}.$$

The following definitions and constants are used

$$\tau = \frac{\tau_t}{C_\mu} = \frac{C_\mu^{1/4}}{C_\mu}\frac{\left(kL\right)}{k^{3/2}},$$

$$\eta^2 = \left\{S^{*2}\right\},$$

$$\gamma_0^* = \frac{C_1^1}{2}, \quad \gamma_1^* = \frac{C_1^0}{2} + \left(\frac{C_{\varepsilon 2} - C_{\varepsilon 1}}{C_{\varepsilon 1} - 1}\right),$$

$$C_{\varepsilon 1} = 1.44, \quad C_{\varepsilon 2} = 1.83,$$

$$C_1^1 = 1.8, \quad C_1^0 = 3.4,$$

$$C_2 = 0.36, \quad C_3 = 1.25, \quad C_4 = 0.6,$$

$$p = -\frac{\gamma_1^*}{\eta^2\gamma_0^*},$$

$$q = \frac{1}{\left(2\eta^2\gamma_0^*\right)^2}\left(\gamma_1^{*2} - 2\eta^2\gamma_0^* a_1 - \frac{2}{3}\eta^2 a_3^2 - 2R^2\eta^2 a_2^2\right),$$

$$r = \frac{\gamma_1^* a_1}{\left(2\eta^2\gamma_0^*\right)^2},$$

$$\left\{W^{*2}\right\} = -W_{ij}^* W_{ij}^*, \quad R^2 = -\frac{\left\{W^{*2}\right\}}{\left\{S^{*2}\right\}}.$$

The root with the smallest real part is chosen from Eq. (12). If $\eta^2 < 10^{-6}$, then

$$\alpha = -\frac{\gamma_1^* a_1}{\gamma_1^{*2} - 2\left\{W^{*2}\right\}a_2^2}.$$

Otherwise, define

$$\alpha = q - \frac{p^2}{3}, \quad b = \frac{1}{27}\left(2p^3 - 9pq + 27r\right), \quad d = \frac{b^2}{4} + \frac{a^3}{27}.$$

If $d > 0$, then

$$t_1 = \left(-\frac{b}{2} + \sqrt{d}\right)^{1/3}, \quad t_2 = \left(-\frac{b}{2} - \sqrt{d}\right)^{1/3},$$

$$\alpha = \min\left(-\frac{p}{3} + t_1 + t_2, -\frac{p}{3} - \frac{t_1}{2} - \frac{t_2}{2}\right).$$

Else, if $d \le 0$,

$$\theta = \cos^{-1}\left(-\frac{b}{2\sqrt{\frac{a^3}{27}}}\right),$$

$$t_1 = -\frac{p}{3} + 2\sqrt{-\frac{a}{3}}\cos\left(\frac{\theta}{3}\right), \quad t_2 = -\frac{p}{3} + 2\sqrt{-\frac{a}{3}}\cos\left(\frac{2\pi}{3} + \frac{\theta}{3}\right), \quad t_3 = -\frac{p}{3} + 2\sqrt{-\frac{a}{3}}\cos\left(\frac{4\pi}{3} + \frac{\theta}{3}\right),$$

$$\alpha = \min\left(t_1, t_2, t_3\right).$$

For the nonlinear two-equation turbulence models, C_{13} in Eq. (8) is set to 0.25 and C_w in Eq. (1) is set to 1.5. The kL production term, P_{kL} is limited by the production based on the strain rate S,

$$P_k = \tau_{ij}\frac{\partial u_i}{\partial x_j}, \quad P_{kL} = \max\left(P_k, \mu_t^L S^2\right), \quad \mu_t^L = C_\mu^{1/4}\frac{\rho\left(kL\right)}{k^{1/2}}. \tag{13}$$

The original Speziale-Sarkar-Gatski (SSG)[44] model used a value of 0.8 for a_2. In the kL-based models, a_2 is set to 0.7, which is based on calibration done to improve the 2D NASA Hump test case.[27] The change in a_2 is within the recommended value of 0.5 to 0.85. Modification in a_2 and the limiting of P_{kL} improved the results for several cases with flow separation, which are reported Ref. [27].

C. k-kL-QCR Model

The k-kL-QCR is based on Spalart's Quadratic Constitutive Relation[39] and is given by,

$$\tau_{ij}^{k-kL-QCR} = -\rho k\left[\beta_1 T^{(1)} + \beta_4 T^{(4)} + \frac{2}{3}\delta_{ij}\right] = \tau_{ij} - C_{cr1}\left(Q_{ik}\tau_{jk} + Q_{jk}\tau_{ik}\right) \tag{14}$$

$$Q_{ik} = \frac{2W_{ik}}{\sqrt{\frac{\partial u_m}{\partial x_n}\frac{\partial u_m}{\partial x_n}}}, \quad \beta_1 = -2 * 0.09, \quad \beta_4 = \frac{2\beta_1 C_{cr1}}{\tau\sqrt{\frac{\partial u_m}{\partial x_n}\frac{\partial u_m}{\partial x_n}}} \tag{15}$$

The constant, $C_{cr1} = 0.3$.

D. SA-RC-QCR2000 Scheme

The Spalart-Allmaras (SA)[37] scheme with modifications to model the rotation and curvature effects (RC)[38], and the computation of nonlinear turbulent stresses using Quadratic Constitutive Relation (QCR)[39] is described in this section. The SA-RC-QCR2000 model was used along with wind tunnel measurements in the evaluation of k-kL schemes. The SA-based schemes are described in detail on the NASA LaRC's Turbulence Modeling Resource (TMR)[35] website – the TMR description is reproduced here almost verbatim for the sake of completeness. The standard baseline SA model is a linear eddy viscosity model based on the Boussinesq assumption, given by

$$\frac{\partial \tilde{\nu}}{\partial t} + u_j \frac{\partial \tilde{\nu}}{\partial x_j} = c_{b1}\left(1 - f_{t2}\right)\tilde{S}\tilde{\nu} - \left[c_{w1} f_w - \frac{c_{b1}}{\kappa^2} f_{t2}\right]\left(\frac{\tilde{\nu}}{d}\right)^2 + \frac{1}{\sigma}\left[\frac{\partial}{\partial x_j}\left(\left(\nu + \tilde{\nu}\right)\frac{\partial \tilde{\nu}}{\partial x_j}\right) + c_{b2}\frac{\partial \tilde{\nu}}{\partial x_i}\frac{\partial \tilde{\nu}}{\partial x_i}\right]. \tag{16}$$

The turbulent eddy viscosity μ_t, is computed using the following relation

$$\mu_t = \rho \tilde{\nu} f_{v1}, \tag{17}$$

where,

$$f_{v1} = \frac{\chi^3}{\chi^3 + c_{v1}^3}, \quad \chi = \frac{\tilde{\nu}}{\nu}, \tag{18}$$

ρ is the fluid density, $\nu = \frac{\mu}{\rho}$ is the kinematic viscosity, and μ is the dynamic viscosity. Various functions and constants used in the formulation are listed below

$$\tilde{S} = \Omega + \frac{\tilde{\nu}}{\kappa^2 d^2} f_{v2}, \tag{19}$$

where $\Omega = \sqrt{2W_{ij}W_{ij}}$ is the magnitude of the vorticity, and d is the distance to the nearest wall.

$$f_{v2} = 1 - \frac{\chi}{1 + \chi f_{v1}}, \quad f_w = g\left[\frac{1 + c_{w3}^6}{g^6 + c_{w3}^6}\right]^{1/6}, \tag{20}$$

$$g = r + c_{w2}\left(r^6 - r\right), \quad r = \min\left[\frac{\tilde{\nu}}{\tilde{S}\kappa^2 d^2}, 10\right], \quad f_{t2} = c_{t3}\exp\left(-c_{t4}\chi^2\right),$$

$$c_{b1} = 0.1355, \quad \sigma = 2/3, \quad c_{b2} = 0.622, \quad \kappa = 0.41,$$

$$c_{w2} = 0.3, \quad c_{w3} = 2, \quad c_{v1} = 7.1, \quad c_{t3} = 1.2, \quad c_{t4} = 0.5, \quad c_{w1} = \frac{c_{b1}}{\kappa^2} + \frac{1 + c_{b2}}{\sigma}.$$

The wall and the farfield boundary conditions are prescribed as follows,

$$\tilde{\nu}_{wall} = 0, \quad \tilde{\nu}_{farfield} = \left[3\nu_\infty, 5\nu_\infty\right]. \tag{21}$$

The $\tilde{\nu}$ boundary conditions corresponding to the turbulent kinematic viscosity values are as follows,

$$\tilde{\nu}_{t,wall} = 0, \quad \tilde{\nu}_{t,farfield} = \left[0.210438\nu_\infty, 1.294234\nu_\infty\right]. \tag{22}$$

FUN3D uses the lower bounds of $3\nu_\infty$ and $0.210438\nu_\infty$ at the farfield. The rotation and curvature (SA-RC) effects are included in the standard SA following Spalart and Shur[38] by including the rotation function,

$$f_{r1} = \left(1 + c_{r1}\right)\frac{2r^*}{1 + r^*}\left[1 - c_{r3}\tan^{-1}\left(c_{r2}\tilde{r}\right)\right] - c_{r1}. \tag{23}$$

The first term on the right hand side of the standard SA equation becomes $c_{b1}\left(f_{r1} - f_{t2}\right)\tilde{S}\tilde{\nu}$. The different terms and constants in Eq. (23) are,

$$r^* = \frac{S}{\omega}, \quad \tilde{r} = \frac{2\omega_{ik}S_{jk}}{D^4}\left(\frac{DS_{ij}}{Dt} + \left(\varepsilon_{imn}S_{jn} + \varepsilon_{jmn}S_{in}\right)\Omega'_m\right),$$

$$\omega_{ij} = \frac{1}{2}\left[\left(\frac{\partial u_i}{\partial x_j} - \frac{\partial u_j}{\partial x_i}\right) + 2\varepsilon_{mji}\Omega'_m\right], \quad S^2 = 2S_{ij}S_{ij}, \quad \omega^2 = 2\omega_{ij}\omega_{ij}, \quad D^2 = \frac{1}{2}\left(S^2 + \omega^2\right),$$

$$c_{r1} = 1.0, \quad c_{r2} = 12, \quad c_{r3} = 1.0,$$

where, DS_{ij}/Dt is the Lagrangian derivative of the strain rate tensor. The rotation rate Ω' is used only when the reference frame is also rotating. The Lagrangian derivative is given by

$$\frac{DS_{ij}}{Dt} \equiv \frac{\partial S_{ij}}{\partial t} + u_k\frac{\partial S_{ij}}{\partial x_k}.$$

The nonlinear Quadratic Constitutive Relation (QCR)[39] modification of the turbulent stress is defined by

$$\tau_{ij}^{QCR} = \tau_{ij} - C_{cr1}\left[O_{ik}\tau_{jk} + O_{jk}\tau_{ik}\right], \tag{24}$$

where τ_{ij} are the turbulent stresses using the Boussinesq assumption, and O_{ik} is an antisymmetric normalized rotation tensor,

$$O_{ik} = \frac{2W_{ik}}{\sqrt{\dfrac{\partial u_m}{\partial x_n}\dfrac{\partial u_m}{\partial x_n}}},$$

and,

$$W_{ik} = \frac{1}{2}\left(\frac{\partial u_i}{\partial x_k} - \frac{\partial u_k}{\partial x_i}\right), \quad \sqrt{\frac{\partial u_m}{\partial x_n}\frac{\partial u_m}{\partial x_n}} = \sqrt{u_x^2 + u_y^2 + u_z^2 + v_x^2 + v_y^2 + v_z^2 + w_x^2 + w_y^2 + w_z^2}.$$

The constant $C_{cr1} = 0.3$.

The TMR notation SA-RC-QCR2000 is kept in the text but has been simplified to SARC-QCR for the plots.

V. Evaluation of the k-kL Formulations

The reference Reynolds number (Re_c) in the tunnel based on the crank chord was fixed at 2.4 million. In the simulations, Re_c/mm is specified, which was set to 4307.4515 based on the chord length. The 14x22 wind tunnel does not have a temperature controller and in order to maintain a constant Reynolds number, the tunnel velocity was adjusted to account for changes in the temperature, which varied from 275 K to 308 K. In the simulations, the reference temperature was set to 288.84 K. The Mach number in the tunnel varied from 0.175 to 0.205 from run to run and in the simulations it was set to 0.189. The angle of attack for –2.5° configuration varied from –2.54° to –2.48° and was set to –2.5° in the simulations. Similarly, there was a variation from 4.97° to 5.04° for the 5.0° angle of attack case and for the simulations it was set to 5.0°. The reference conditions are given in Table 1.

Table 1: Reference Conditions.

Parameter	FUN3D	Tunnel Conditions
Mach Number	0.189	0.175 to 0.205
Reynolds Number	Re_c/mm=4307.4515	$Re_c = 2.4\times10^6 \pm 0.3\%$
T_{ref}	288.84 K	275 to 308 K
α_1	–2.5°	–2.54° to –2.48°
α_2	5°	4.97° to 5.04°

The JF model was built with a truncated DLR-F6 wing with a span of 3397.25 mm and a 27.1° leading edge sweep. The crank chord length was 557.17 mm (located at 759 mm from the fuselage). The fuselage length, height, and width were 4.839 m, 0.67 m, and 0.472 m, respectively. The origin of the coordinates was set at the fuselage nose and the *x*-axis ran along the fuselage centerline. The *y*-axis was in the spanwise direction (positive in the starboard direction). The LDV probes scanned the wing on the port side. The wing-fuselage juncture was at y = –236.1 mm on the port side and the wing root trailing edge was at x = 2961.9 mm.

In order to conduct a grid-convergence study, three unstructured grids of coarse, medium, and fine resolution were generated using Pointwise™ with approximately 12 million, 40 million, and 160 million nodes, respectively. A zoomed view of the wing-fuselage section for the coarse, medium, and fine grids is shown in Figure 2. The grids were generated for a half-span JF model with symmetry boundary condition in the *x*-*z* plane. The computational domain was bounded by $(x, y, z) \in [-55880, 55880] \times [-55880, 0] \times [-55880, 55880]$ mm.

The Roe[45] solver with no flux limiting was used in all simulations. The three variations of the k-kL schemes: baseline k-kL (linear model), k-kL-QCR (k-kL with the quadratic constitutive relation), and k-kL-ARSM (k-kL with the algebraic Reynolds stress model) were evaluated using the JF experiment data, and with the SA-RC-QCR2000 model. In the wind tunnel test the flow was tripped at x = 336 mm from the nose as well as on the upper and lower wing surfaces, therefore, all CFD simulations were run in the fully turbulent mode.

Convergence (8-9 orders of magnitude reduction in the residuals) was achieved in around 40,000 iterations for a k-kL run on the medium mesh. The k-kL-QCR runs also showed similar behavior. The k-kL-ARSM residuals flattened at around 10,000 iterations after 6-7 orders of magnitude reduction in residuals. On the fine mesh, the k-kL-ARSM simulation could not be initialized from a cold start and had to be initialized using the restart data from the k-kL-QCR simulation. Typical timings for the k-kL simulations are given in Table 2.

Table 2: Run Statistics (Roe – k-kL – 40,000 iterations – α=5°).

Mesh	Mesh Size (nodes)	CPUs (Broadwell)	Wallclock (hours)
Coarse	~12 million	2016	3
Medium	~40 million	2016	9
Fine	~160 million	4928	18

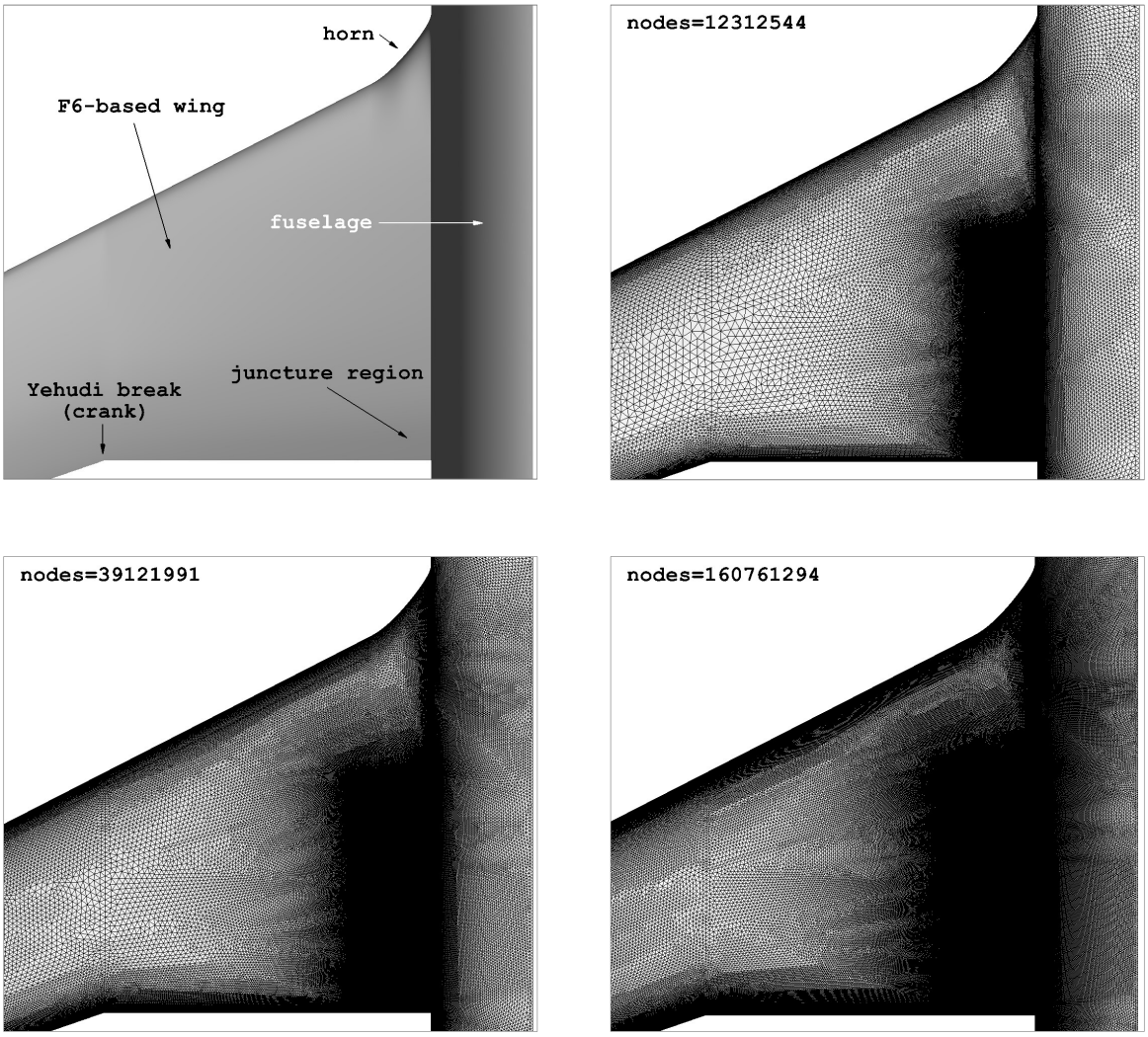

Figure 2. The top row shows a zoomed view of the juncture flow model and the coarse mesh (~12 million nodes). The bottom row shows the medium (~40 million nodes), and the fine (~160 million nodes) meshes used in the grid convergence study.

A. Grid Convergence

The results of the grid convergence study are shown in Figures 3-9. Figures 3 and 5 show the prediction of the separation bubble for the 5° angle of attack case using different turbulence schemes on the coarse, medium, and fine meshes. In general, the width of the bubble shows convergence toward the measured width size for all cases. The length of the separation bubble was overestimated by all models. The best grid convergence behavior was seen in the SA-RC-QCR2000 runs. For the k-kL models, the bubble length increased on the fine resolution meshes. Similar behavior (increase in bubble dimensions with increase in mesh resolution) for some schemes was also reported by Lee and Pulliam[19] in their juncture flow simulations using OVERFLOW. The k-kL-ARSM scheme predicted the smallest bubble size compared to other schemes on coarse and medium grids, however, on the fine mesh resolution, the SA-RC-QCR2000 predicted bubble size was approximately the same as k-kL-ARSM. There were variations in the bubble topology for different schemes. The separation flow features predicted by k-kL and k-kL-ARSM were similar, while the k-kL-QCR and SA-RC-QCR2000 predicted bubbles shared similar topology.

Figures 4 and 6 show the prediction of separation bubble for the –2.5° angle of attack configuration. As expected, the predicted bubble is smaller in size compared to the 5° angle of attack case. The trends for this configuration were similar to the 5° angle of attack case. At fine mesh resolution, the SA-RC-QCR2000 scheme predicts the smallest bubble size.

The prediction of separation initiation location (length of the separation bubble) by the different models for the two cases is listed in Tables 3 and 4 for reference. In general, all models predict early separation (overestimate the bubble length). This might be due to the inability of the models to capture the correct anisotropy in the normal stresses near the wall. In general, there are discrepancies in the prediction of normal stresses and these errors are especially large in the case of $u'u'$ prediction near the wall.

Table 3: Separation Initiation Location (Measured = 2843.5 mm) α = 5°.

Scheme	Coarse (mm)	Medium (mm)	Fine (mm)
k-kL	2766.8	2779.7	2771.9
k-kL-ARSM	2823.2	2823.9	2811.1
k-kL-QCR	2771.8	2779.9	2771.9
SARC-QCR2000	2781.8	2799.3	2811.7

Table 4: Separation Initiation Location (Measured = 2811 mm) α = –2.5°.

Scheme	Coarse (mm)	Medium (mm)	Fine (mm)
k-kL	2832.8	2842.4	2837.5
k-kL-ARSM	2859.1	2858.9	2845.8
k-kL-QCR	2832.8	2838.8	2837.1
SA-RC-QCR2000	2844.3	2855.5	2865.8

Comparison of the simulated profiles of the mean velocities on different resolution grids with the LDV measured data for x = 2892.6 mm, y = –246.1 mm is shown in Figure 7 for α = 5°. This point location is within the separation bubble and 10 mm from the fuselage. The k-kL and SA-RC-QCR2000 schemes show influence of the grid resolution while the k-kL-ARSM and k-kL-QCR profiles do not exhibit much sensitivity to changes in grid resolution. The k-kL-ARSM solution is more accurate compared with other models. The other schemes show significant flow separation, which is not present in the measured profile for this location.

Turbulent stresses are compared with the measured data in Figures 8-9. The differences from the measurements in the predicted normal stresses $u'u'$, $v'v'$, and $w'w'$ were generally larger than the differences in shear stresses $u'v'$, $u'w'$, and $v'w'$ for all models. The prediction of turbulence quantities using the k-kL-ARSM model were more accurate compared to other models.

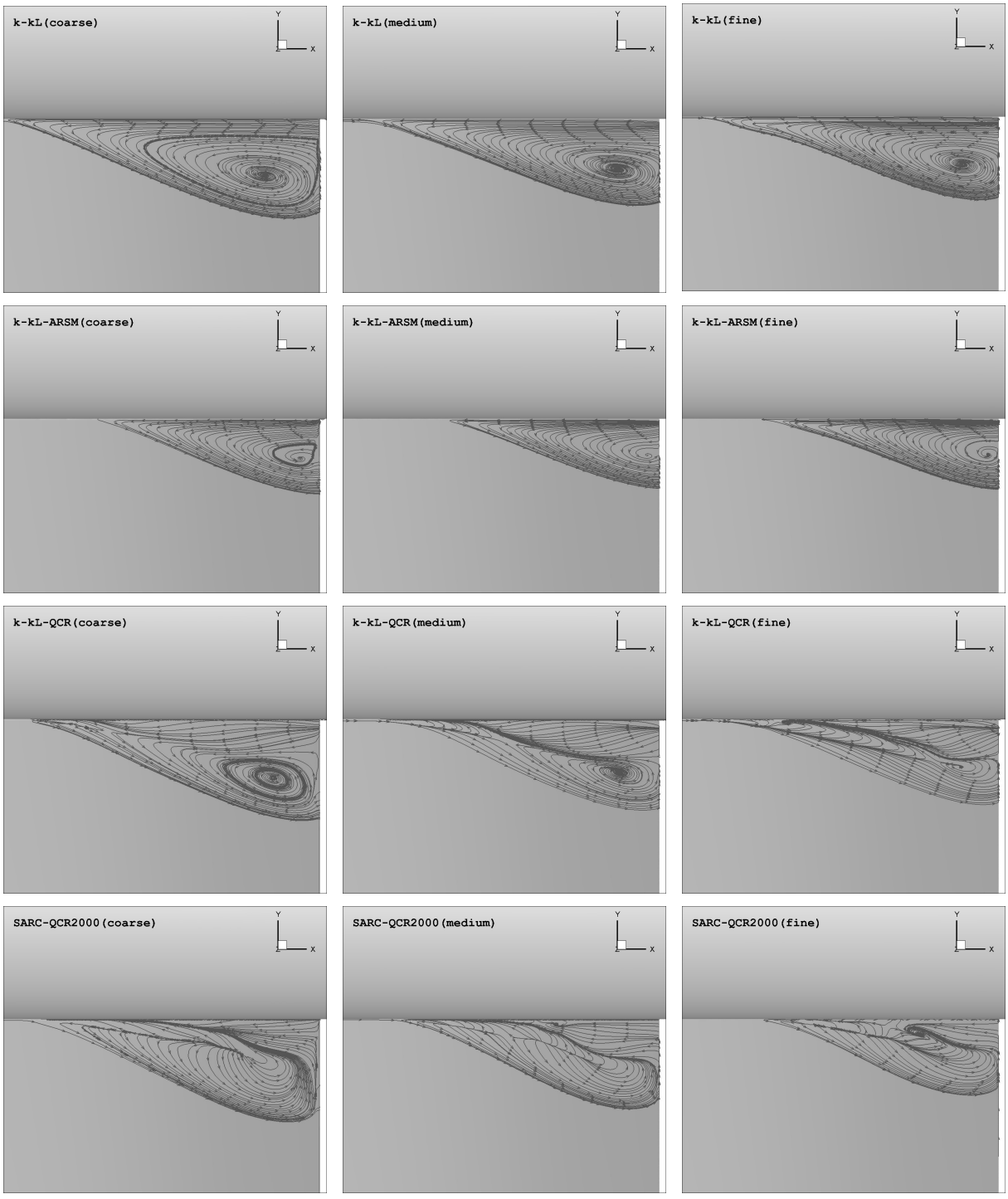

Figure 3. Flow separation in the wing-fuselage juncture region on the coarse, medium, and fine grids using different turbulence models, $\alpha = 5°$.

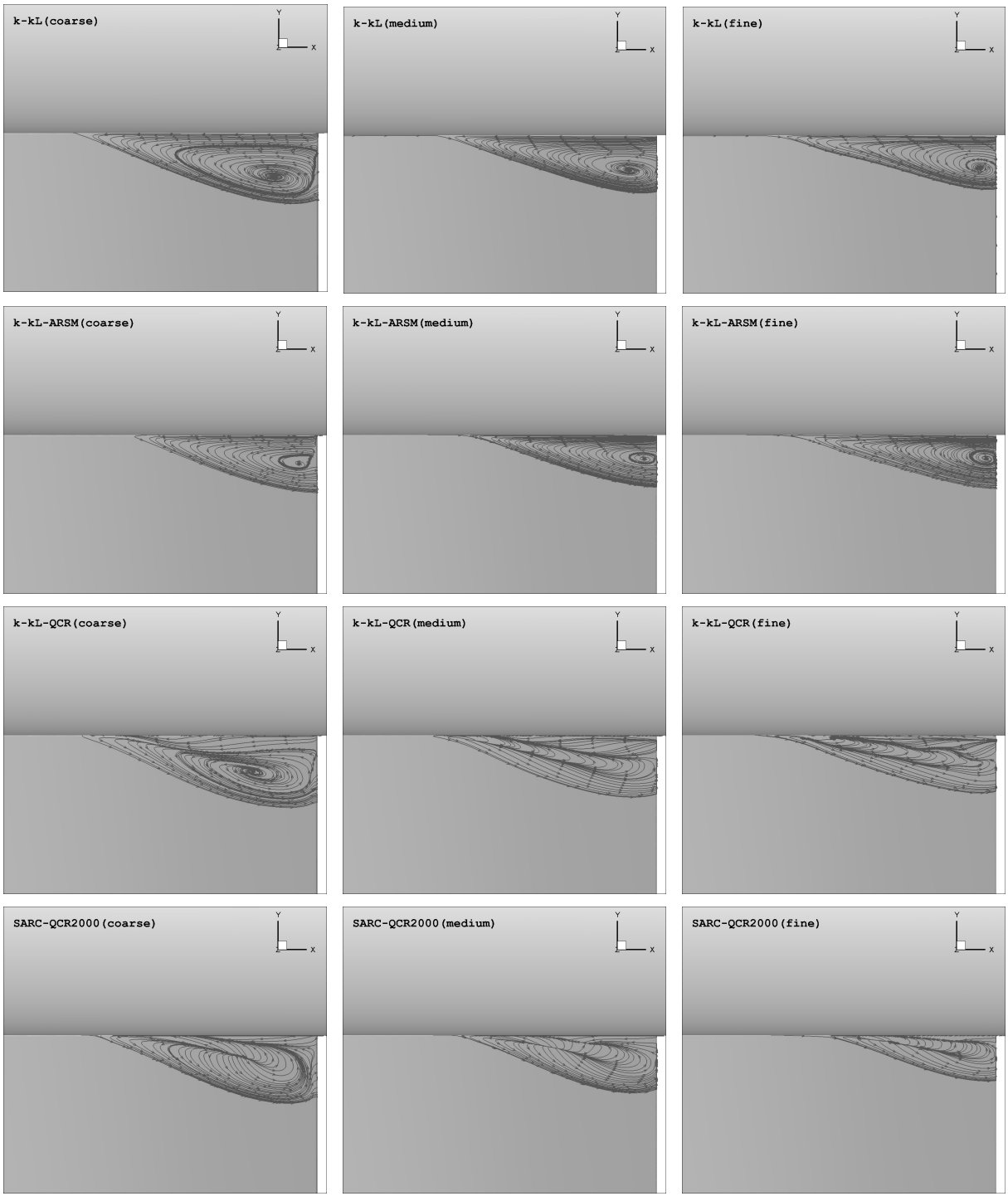

Figure 4. Flow separation in the wing-fuselage juncture region on the coarse, medium, and fine grids using different turbulence models, $\alpha = -2.5°$.

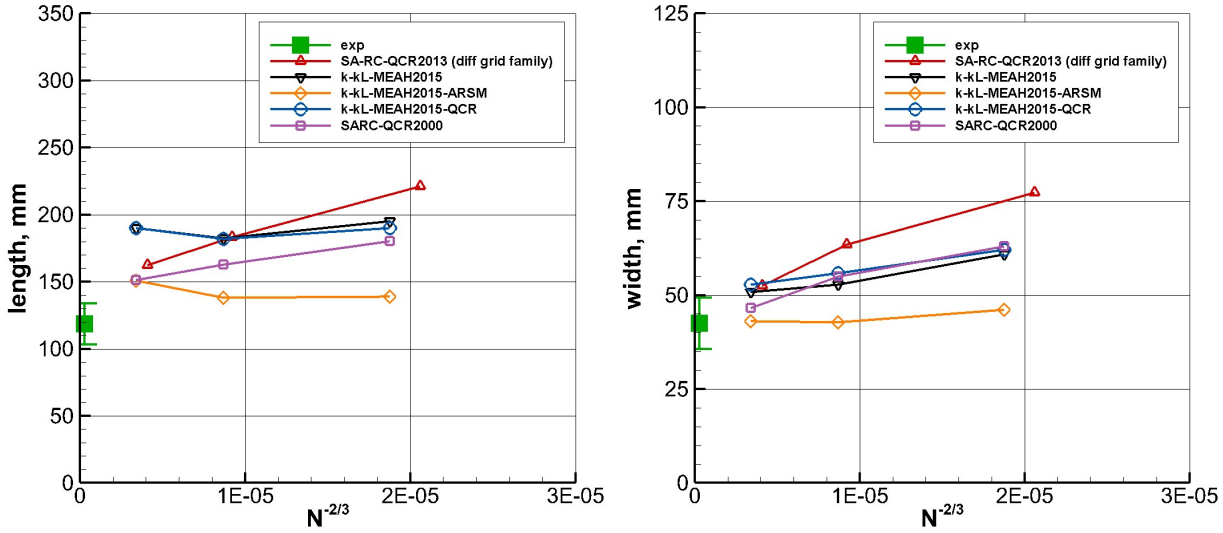

Figure 5. Separation length (left panel) and width (right panel) as a function of the grid size for different turbulence models, α = 5°. The data in red are for SA-RC-QCR2013 from a previous JF study[18] on a different set of grids.

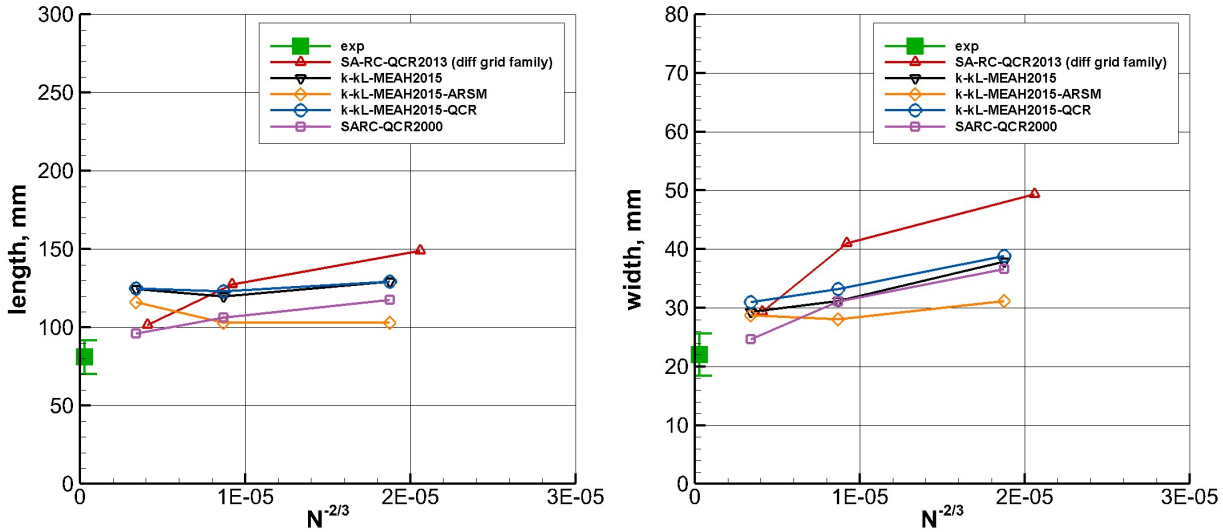

Figure 6. Separation length (left panel) and width (right panel) as a function of the grid size for different turbulence models, α = –2.5°. The data in red are for SA-RC-QCR2013 from a previous JF study[18] on a different set of grids.

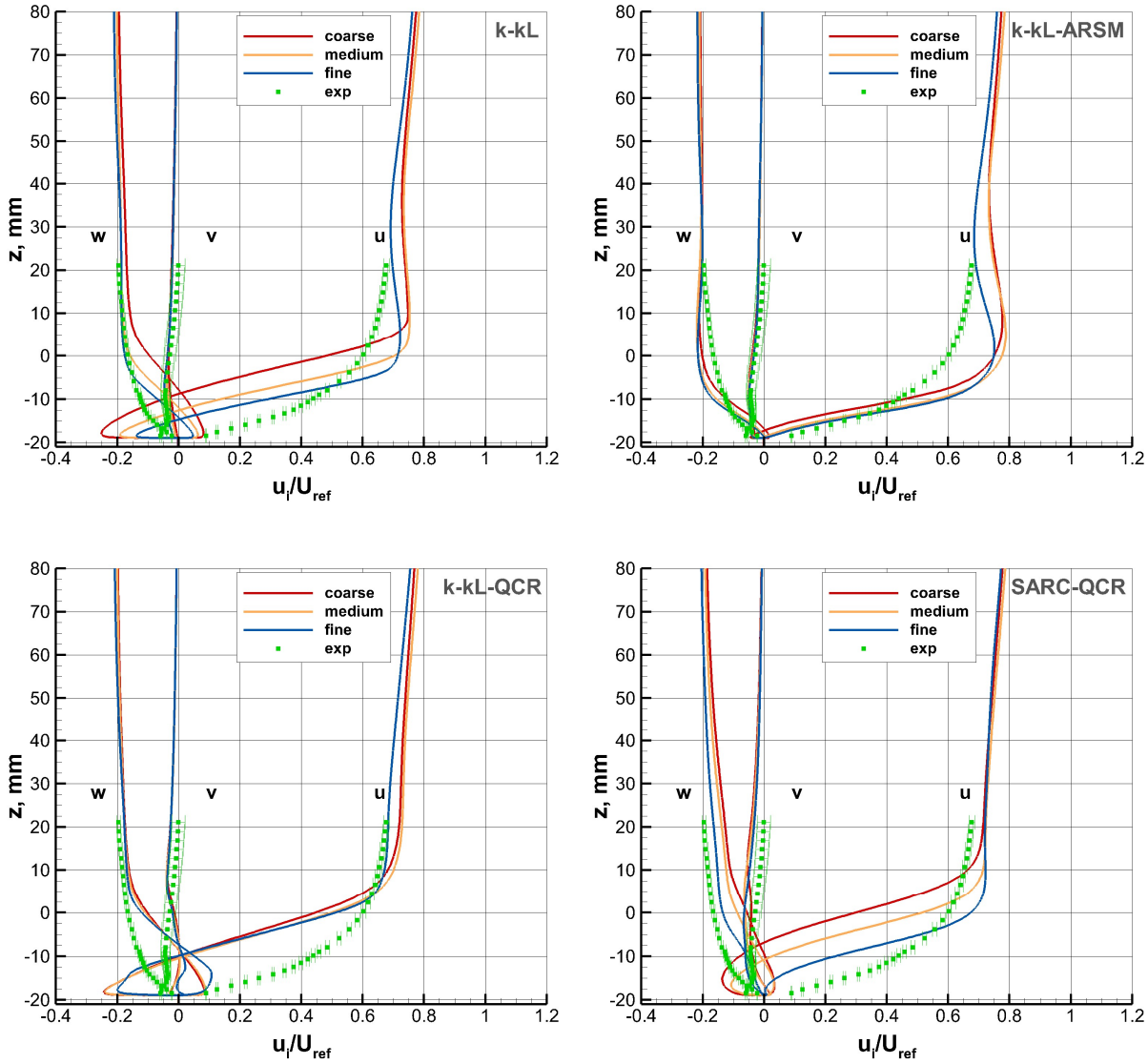

Figure 7. The mean velocity components (*u*, *v*, *w*) on the coarse, medium, and fine grids using different turbulence models, α = 5°, *x* = 2892.6 mm, and *y* = –246.1 mm.

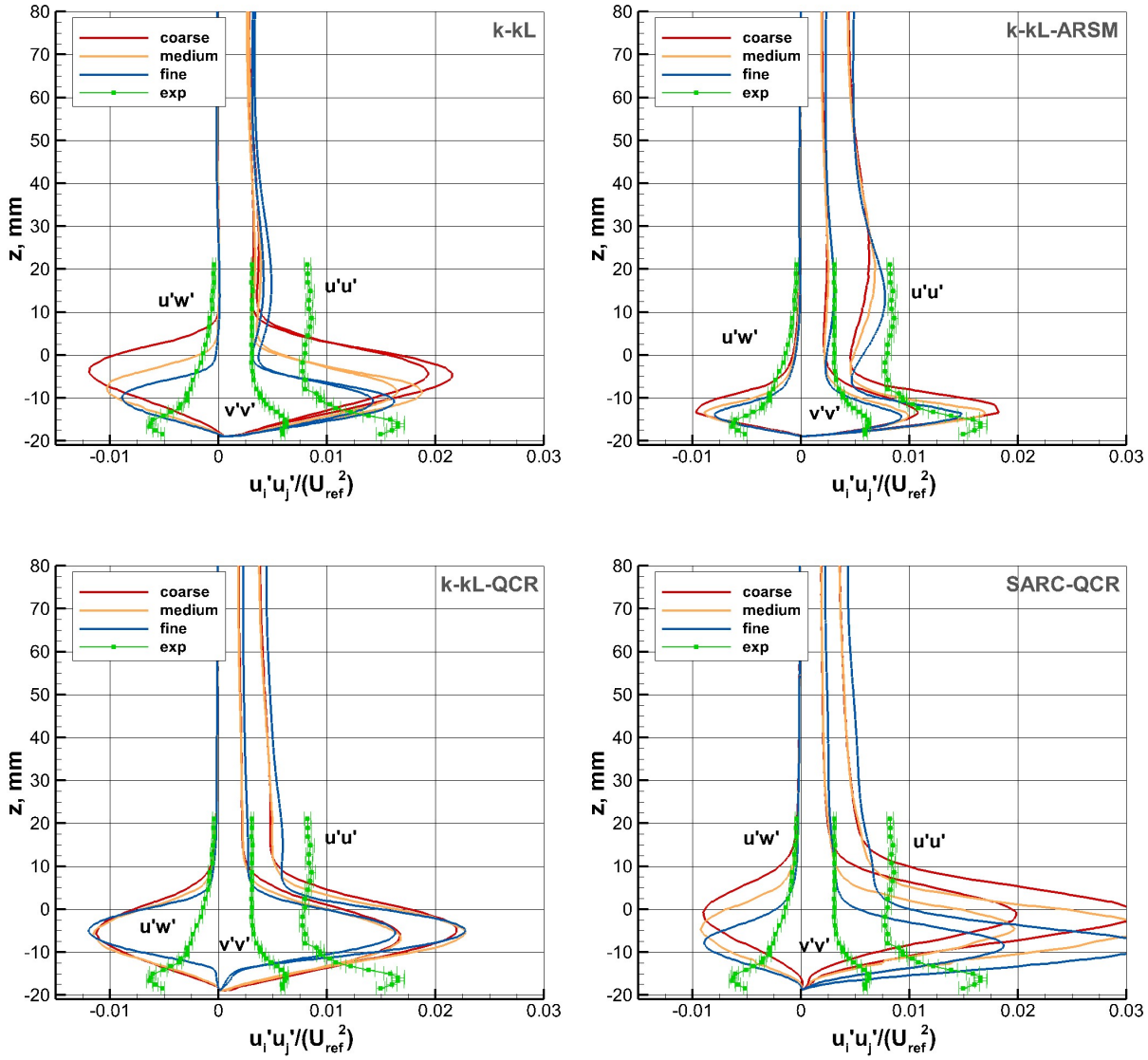

Figure 8. Prediction of turbulence quantities on the coarse, medium, and fine grids using different turbulence models, $\alpha = 5°$, $x = 2892.6$ mm, and $y = -246.1$ mm.

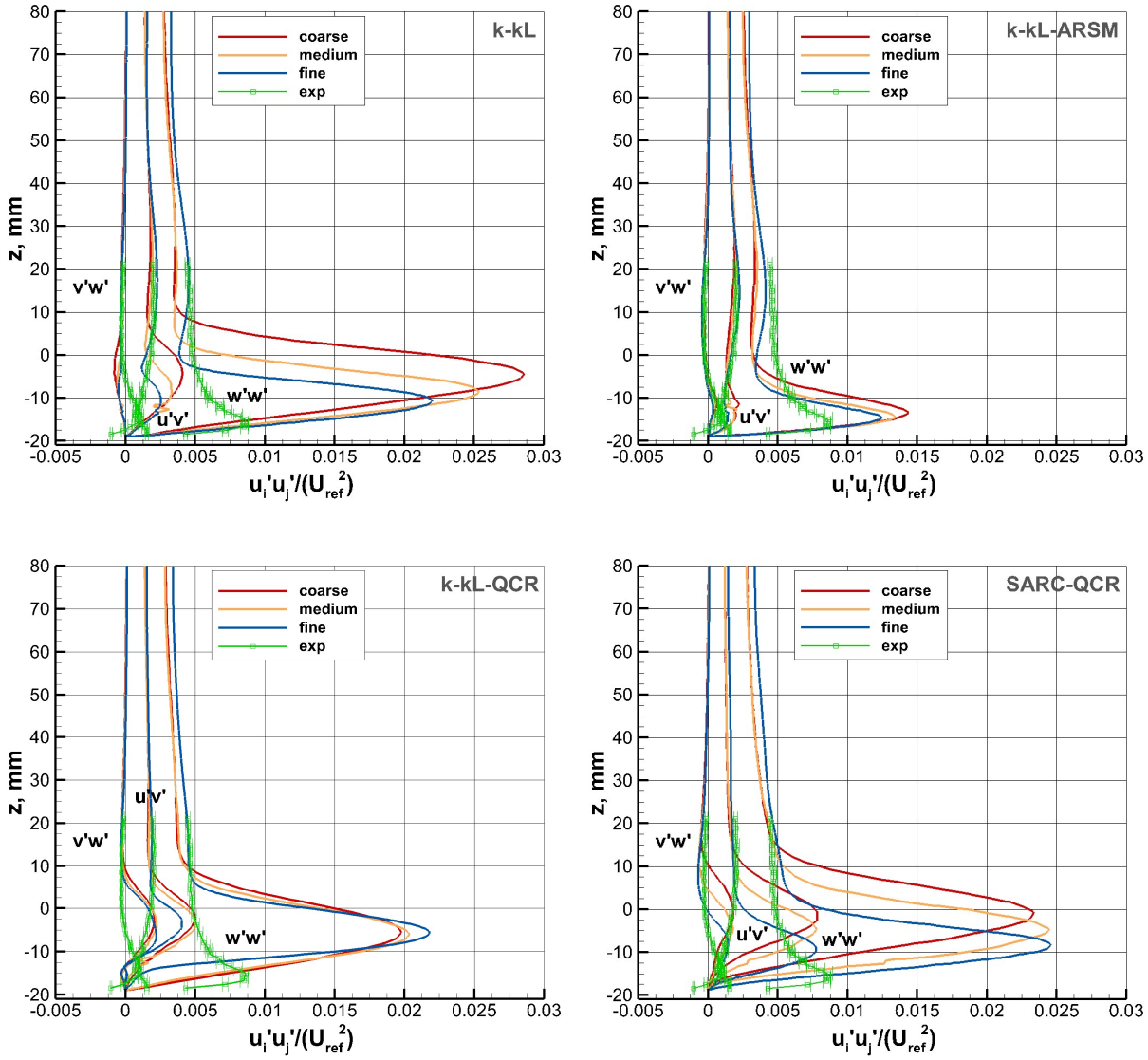

Figure 9. Prediction of turbulence quantities on the coarse, medium, and fine grids using different turbulence models, α = 5°, *x* = 2892.6 mm, and *y* = –246.1 mm.

B. Evaluation of k-kL-ARSM

In the earlier evaluations of the k-kL family of schemes, the k-kL-ARSM had been shown to be the most promising of the three.[27] In this section, the k-kL-ARSM results on the fine mesh are evaluated using the static pressure (C_p) data and the LDV profiles.

Figure 10 shows the comparison of the measured and computed surface pressure coefficients for the 5° angle of attack configuration. Please note that all wind tunnel data (multiple data collection runs for both the port and starboard wings) are plotted in the figure. The scatter in the data can be considered as measurement uncertainty, which is quite small. Overall, the computed C_p values compare well with the measurements. The peaks in C_p at the leading edge of the inboard stations are underestimated by the model, which was also the case in earlier studies.[18-19] The large discrepancy between the computations and the measurements at y = –1663.7 mm is due to lack of sufficient mesh resolution needed to resolve the wingtip vortex.

Figure 11 shows the comparison of mean velocities and turbulence quantities for two points on the fuselage for α = 5°. The location x = 1168.4 mm, z = 0 is closer to the nose, and x = 1859.2 mm, z = 55.05 mm is closer to the wing leading edge. The computed mean velocities are in reasonable agreement with the measurements. With the exception of two components of the normal stresses ($u'u'$, $w'w'$), the rest of the turbulence quantities also match the measurements fairly well.

Figure 12 shows the comparison of computed results with the measurements at two locations on the wing just before the onset of flow separation (x = 2747.6 mm, y = –237.1 mm, and x = 2747.6 mm, y = –266.1 mm). Results are for the angle of attack, α = 5° case. Overall, the mean velocities are again in reasonable agreement with the data. There is some discrepancy in the prediction of the u component profile. The turbulence quantities with the exception of $u'u'$, and $w'w'$ compare well with the measurements. The SA-RC-QCR2013 results reported in [18] showed better prediction of $w'w'$ component for x = 2747.6 mm, y = –237.1 mm, but the model underestimated it for x = 2747.6 mm, y = –266.1 mm.

Similar results are obtained for the α = –2.5° case shown in Figures 13-14. Figure 13 shows the comparison for two points on the fuselage, and Figure 14 shows the comparison for two locations on the wing. Computed mean velocities are in reasonable agreement with the measurements. The small differences observed in the v component of the mean velocity are within the uncertainty bounds of the measurements. In this case also, the model has differences in the prediction of normal stresses compared with measurements and these differences are especially large in $u'u'$ near the wall.

C. Comparison of k-kL-ARSM with k-kL-QCR

The k-kL-ARSM scheme is compared with the k-kL-QCR scheme in Figure 15 at two locations on the wing slightly upstream of the separation bubble at x = 2747.6 mm, y = –237.1 mm, which is 1 mm away from the fuselage, and x = 2747.6 mm, y = –266.1 mm (30 mm away from the fuselage). Computations on the fine mesh for α = 5° case are shown in the figure. With the exception of the u component profile and the w component profile near the wall, the computed mean velocities are in reasonable agreement with the measurements.

The predictions by the two models are not distinctly different. Both models have difficulty predicting the $u'u'$ normal stress component. The predictions of $w'w'$ component are better for the location closer to the fuselage.

D. Comparison of k-kL-QCR with SA-RC-QCR2000

The k-kL-QCR scheme is compared with the SA-RC-QCR2000 scheme in Figure 16 at the same two locations as in Figure 15. Computations on the fine mesh for α = 5° are shown in the figure. As in the previous case, with the exception of the u component, the computed mean velocities are in reasonable agreement with the measurements. The w component is better predicted by SA-RC-QCR2000 at y = –237.1 mm near the wall and the k-kL-QCR prediction shows larger differences from measurements in the w component near the wall at this location. The SA-RC-QCR2000 underestimates the u component at x = 2747.6 mm, y = –266.1 mm, and k-kL-QCR overestimates it.

In this comparison also, the models showed large errors in the prediction of the $u'u'$ normal stress component, especially near the wall. The predictions of $w'w'$ were better at the location closer to the fuselage.

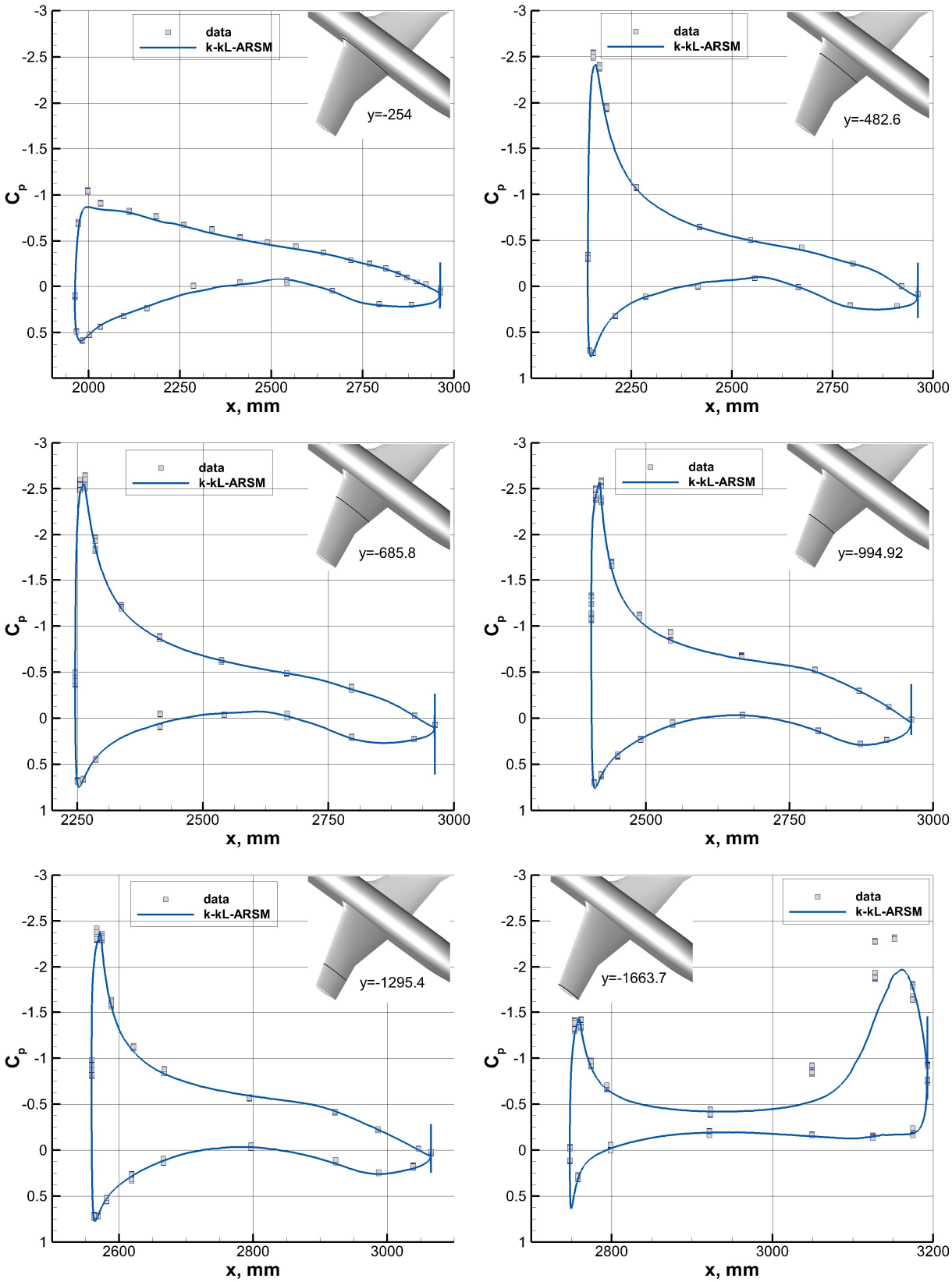

Figure 10. Pressure coefficients on the wing, α = 5°, fine mesh, and k-kL-ARSM model.

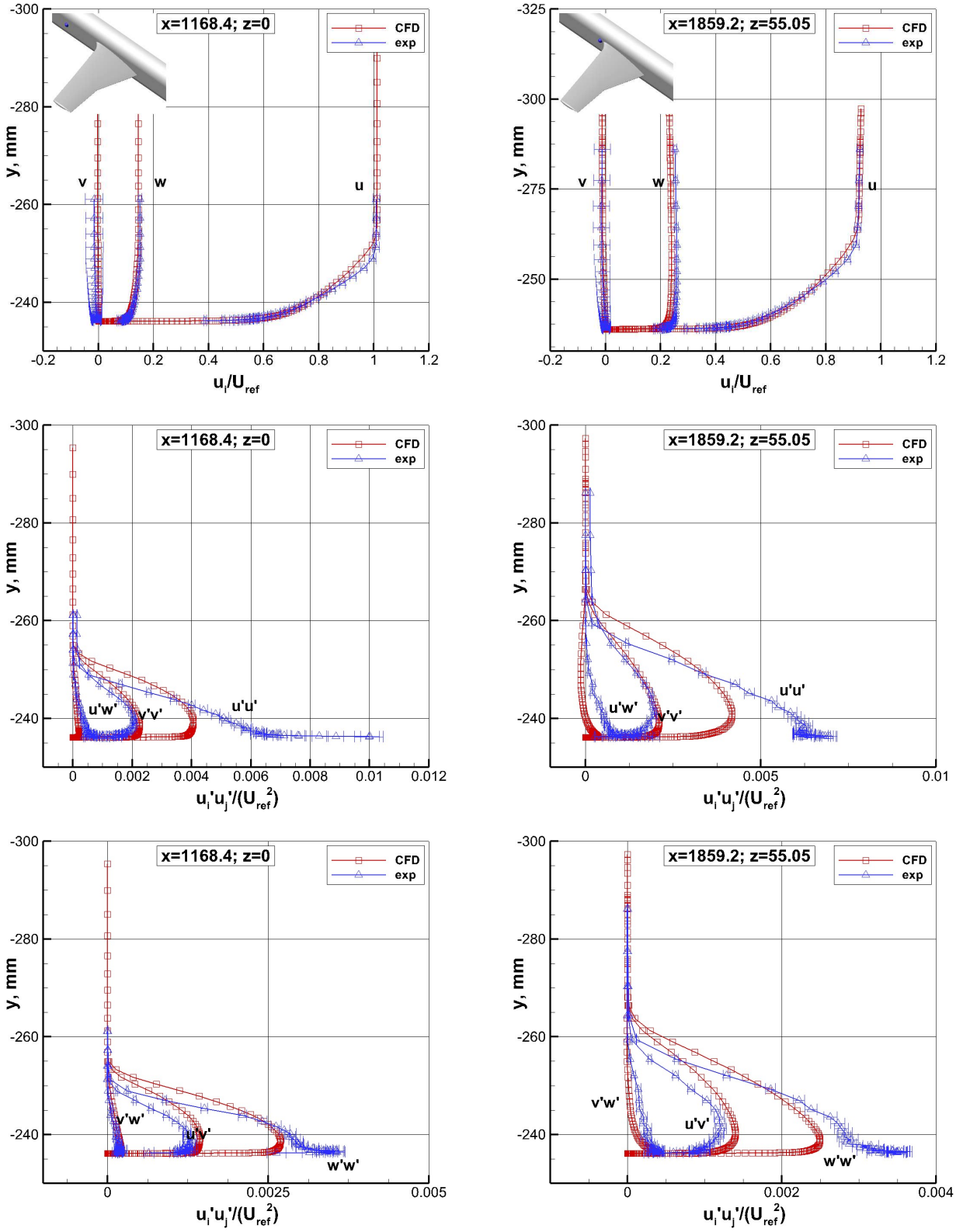

Figure 11. Comparison of the k-kL-ARSM results with the LDV data, fine mesh, α = 5°. Results are shown for (*x*, *z*) = (1168.4 mm, 0), and (*x*, *z*) = (1859.2 mm, 55.05 mm) in the left and the right columns, respectively.

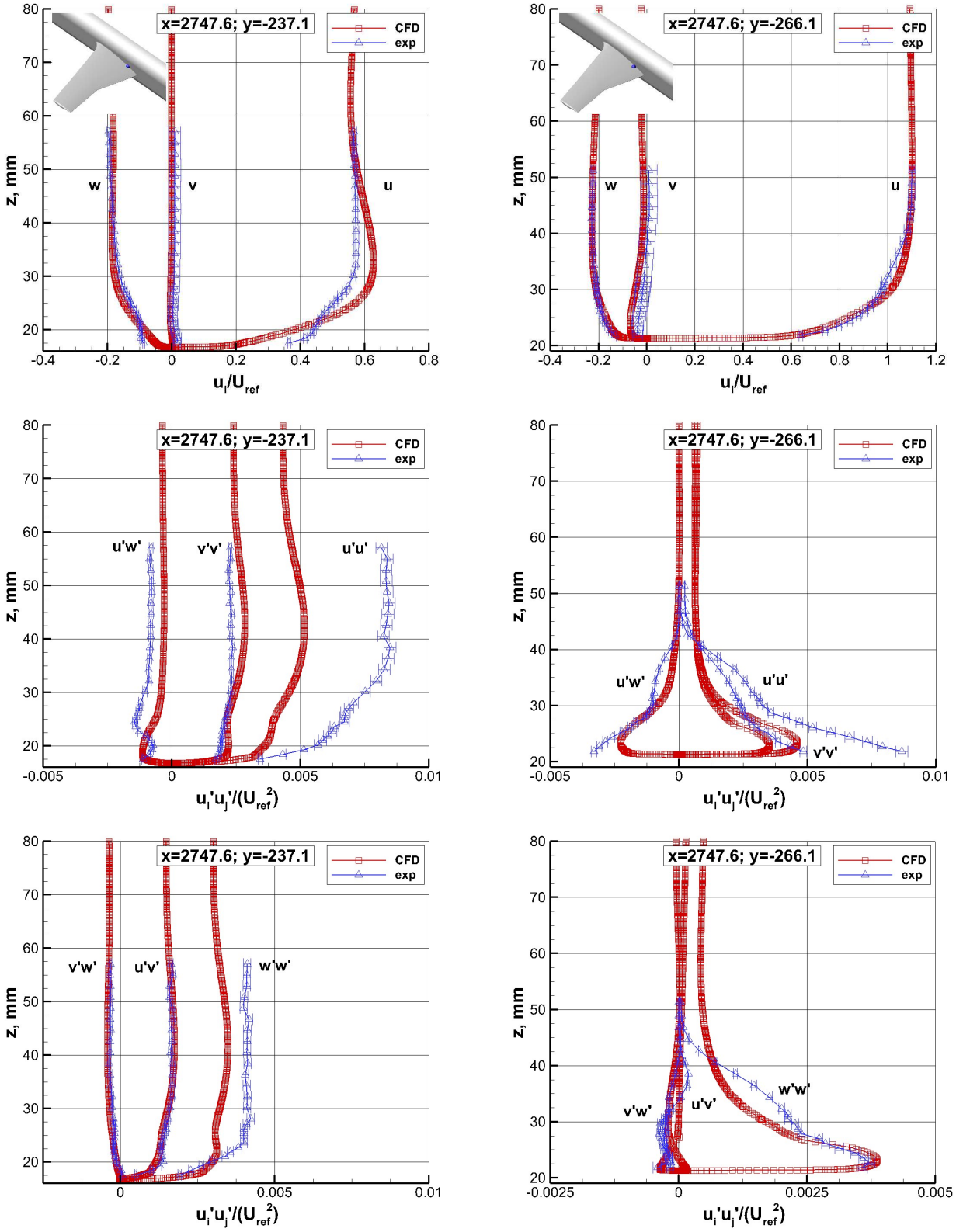

Figure 12. Comparison of the k-kL-ARSM results with the LDV data, fine mesh, α = 5°. Results are shown for (*x*, *y*) = (2747.6 mm, –237.1 mm), and (*x*, *y*) = (2747.6 mm, –266.1 mm) in the left and the right columns, respectively.

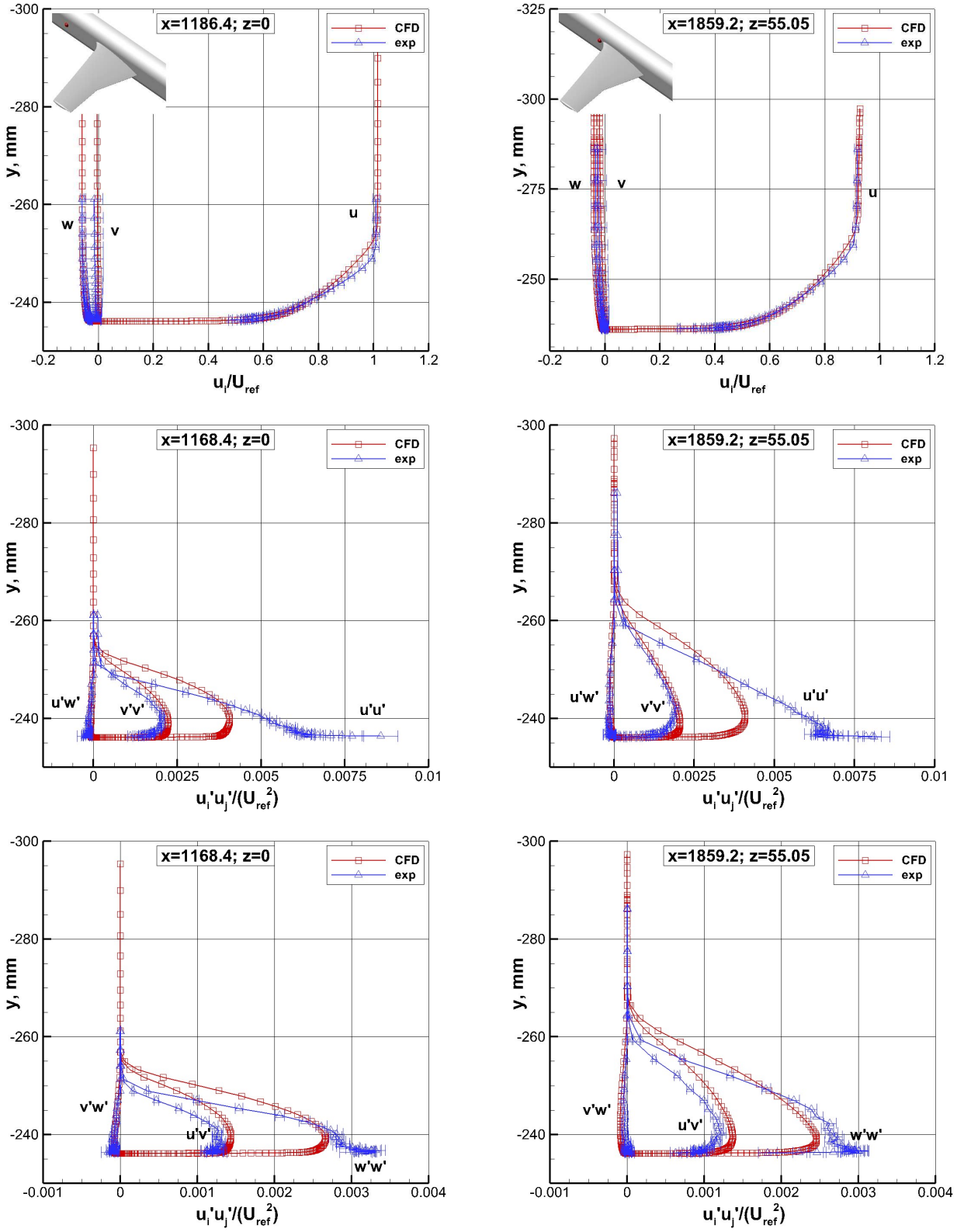

Figure 13. Comparison of the k-kL-ARSM results with the LDV data, fine mesh, α = –2.5°. Results are shown for (*x*, *z*) = (1168.4 mm, 0), and (*x*, *z*) = (1859.2 mm, 55.05 mm) in the left and the right columns, respectively.

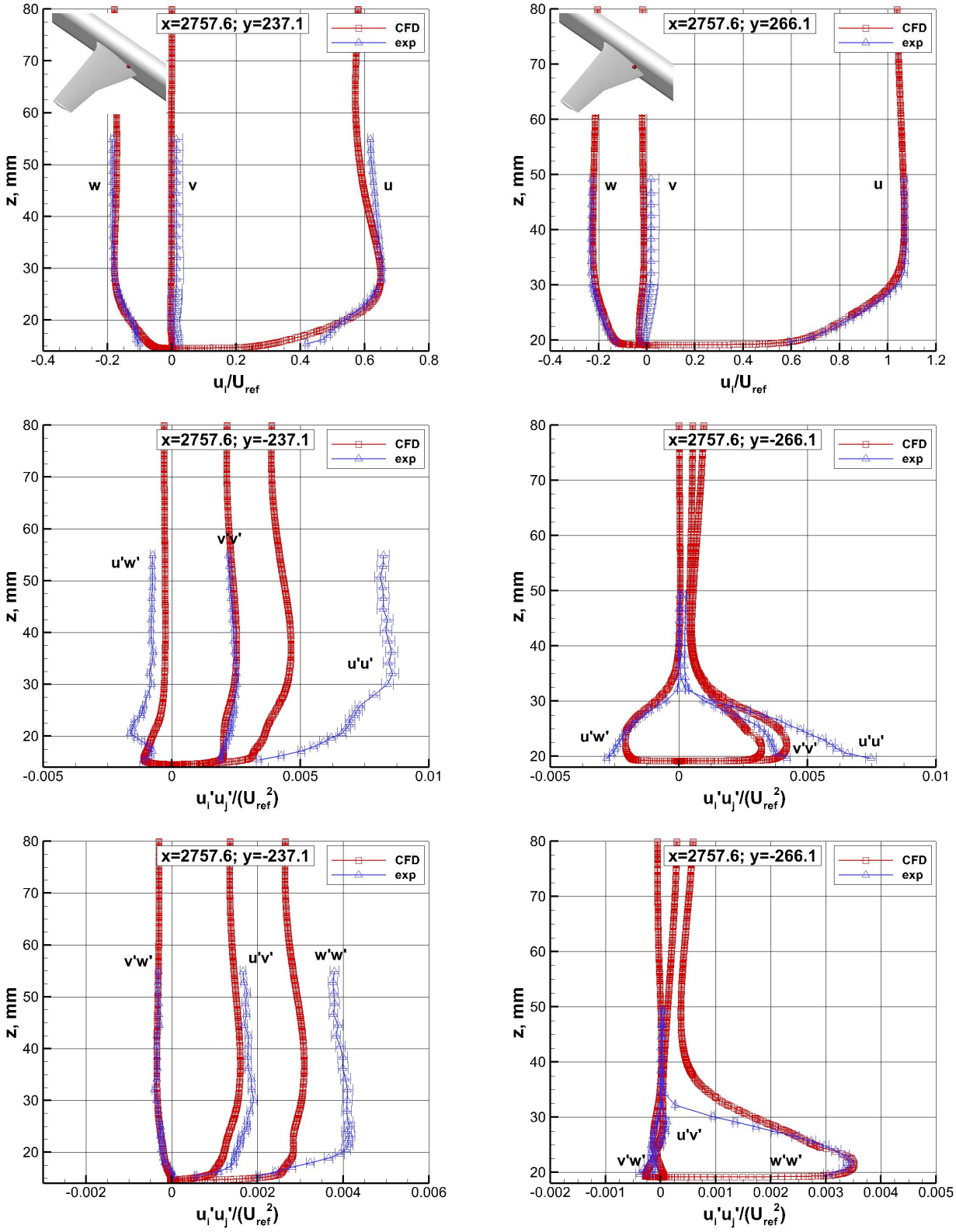

Figure 14. Comparison of the k-kL-ARSM results with the LDV data, fine mesh, α = –2.5°. Results are shown for (*x*, *y*) = (2757.6 mm, –237.1 mm), and (*x*, *y*) = (2757.6 mm, –266.1 mm) in the left and the right columns, respectively.

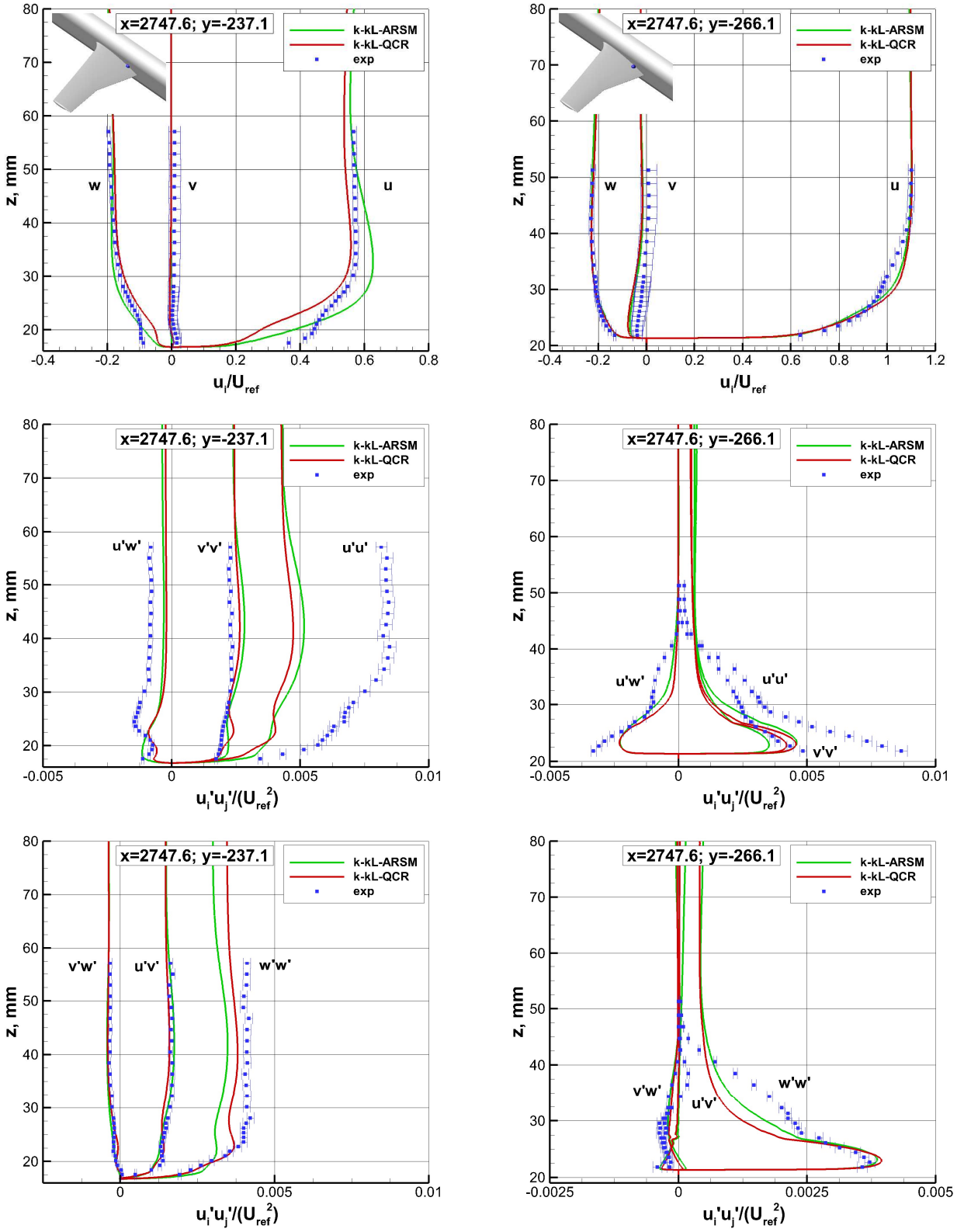

Figure 15. Comparison of k-kL-ARSM with k-kL-QCR, fine mesh, α = 5°. Results are shown for the two schemes at (*x*, *y*) = (2747.6 mm, –237.1 mm), and (*x*, *y*) = (2747.6 mm, –266.1 mm) in the left and the right columns, respectively.

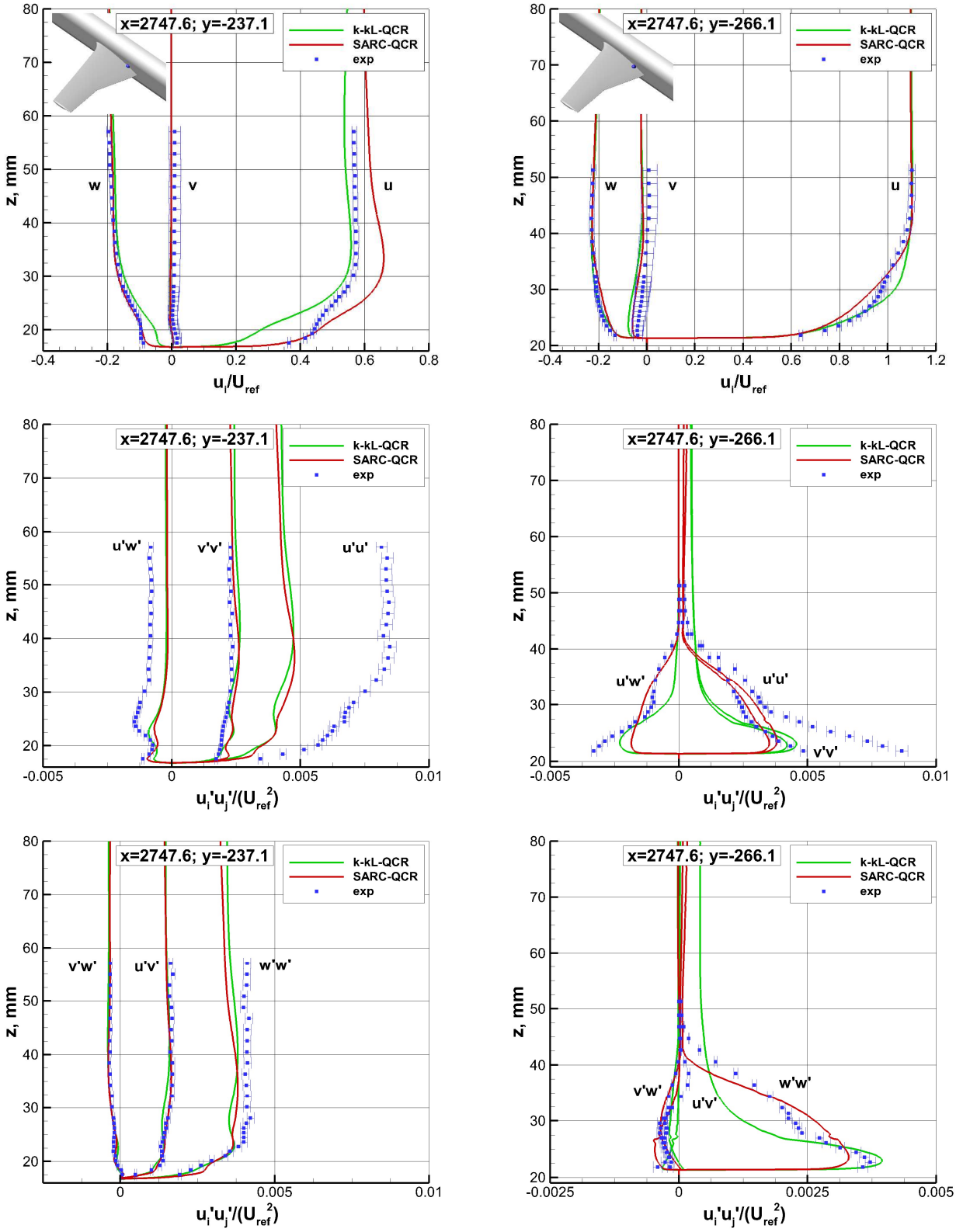

Figure 16. Comparison of k-kL-QCR with SA-RC-QCR2000, fine mesh, α = 5°. Results are shown for the two schemes at (*x*, *y*) = (2747.6 mm, –237.1 mm), and (*x*, *y*) = (2747.6 mm, –266.1 mm) in the left and the right columns, respectively.

VI. Discretization Uncertainty

Grid resolution-based uncertainty bounds were calculated using the method proposed by the American Society of Mechanical Engineers (ASME)[46] with minor modifications.[18] The method provides uncertainty bounds due to discretization errors. The solutions on the coarse, medium, and fine grids were used to estimate the error bars shown in Figure 17 for all schemes at a point inside the separation bubble (x = 2822.6 mm; y = –237.1 mm).

The importance of grid quality becomes apparent when these results are compared with the results presented in Rumsey et al.,[18] which used a different family of grids. The overall uncertainty in the solutions is much smaller implying better grid resolution particularly in the corner region of interest.

The k-kL-ARSM and k-kL-QCR schemes are least sensitive to changes in grid resolution and the SA-RC-QCR2000 exhibits the most sensitivity to grid resolution, especially in the boundary layer. The results imply that the changes in the grid resolution are not affecting the solution as much when using k-kL-ARSM and k-kL-QCR schemes as compared to the SA-RC-QCR2000 scheme.

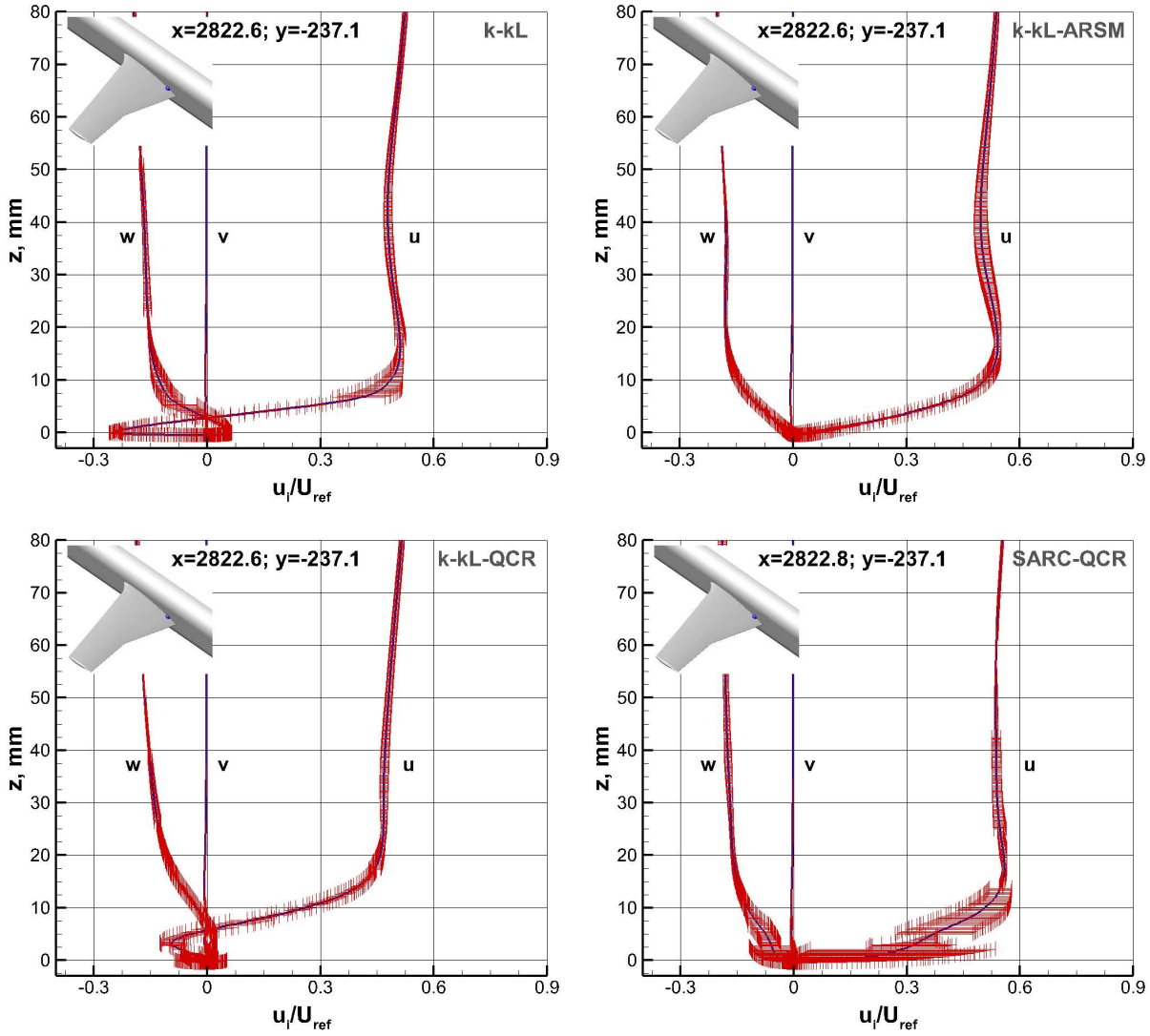

Figure 17. Discretization uncertainty in the mean velocities using k-kL, k-kL-ARSM, k-kL-QCR, and SA-RC-QCR2000 turbulence models, α = 5°, (x, y) = (2822.6 mm, –237.1 mm).

VII. In-Tunnel Simulations

Preliminary results of in-tunnel simulations obtained using FUN3D's overset capabilities are described in this section. The coarse free-air grid from a previous study[18] was reflected across the symmetry plane resulting in a grid for a full-span JF model with approximately 21 million nodes. An empty 14- by 22-foot tunnel grid was rotated by five degrees with respect to the JF model grid – this was done in order to avoid coordinate transformation of measurements for comparison. SUGGAR++[47-48] was used to integrate the JF model full-span grid with the rotated 14x22 grid to obtain the overset grid. The final grid had approximately 29 million nodes. SUGGAR++ generates the grid connectivity information along with the final grid, which is used by FUN3D for interpolation between the two component grids. Figure 18(a) shows the final overset assembly used in the simulation. The locations of the total and static pressure ports with respect to the tunnel wall are shown in Figure 18(b). A zoomed view of the grid is shown in Figure 18(c). Please note that only the portion of the free-air grid on which computations were carried out in the simulation is shown in the figure.

The reference conditions were the same as before and only the baseline k-kL scheme was used for the 5° angle of attack case in this comparison. Usually, for the wind tunnel simulations, the static pressure at the outflow (back pressure) is iterated manually to match the tunnel conditions.[11,12,19] Carlson has automated this procedure in FUN3D using a proportional-integral-derivative (PID) controller.[29] Total pressure measured at the start of the diffuser section and the static pressure measured at the start of the test section are used in the tunnel calibration equations to adjust the back pressure while maintaining the desired tunnel conditions with the help of the PID controller. The location of the total and static pressure probes in the 14x22 wind tunnel are shown in Figure 18(a)-(b). The tunnel conditions in the simulation can be set either in terms of the Reynolds number or the Mach number. In the present simulation, a target Reynolds number equal to the reference Reynolds number was specified. The PID controller was invoked every one thousand iterations to adjust the back pressure boundary condition in order to maintain the target Reynolds number.

The simulation was run for a total of 120,000 iterations. Figure 19 shows the time history of the residuals (mean quantities and turbulence) and the PID controller data. At around 110,000 iterations, the Reynolds number and the Mach number have almost approached the tunnel conditions based on the target Reynolds number. The peaks in the residuals time history correspond to calls to the PID controller routine.

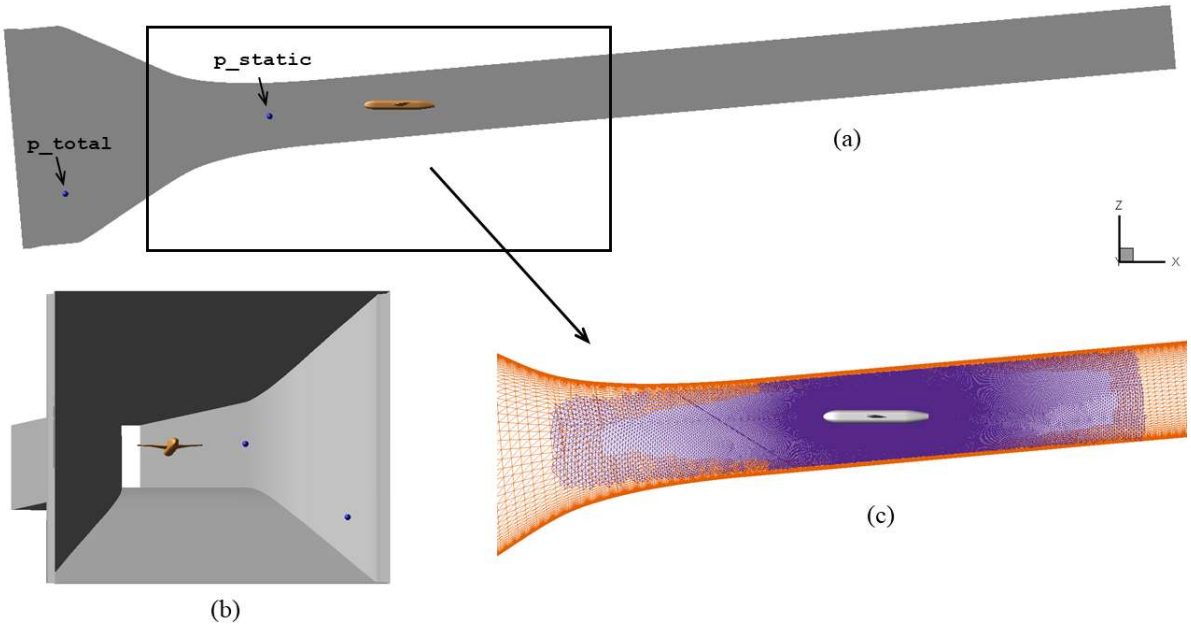

Figure 18. The overset assembly for the Juncture Flow Model in the 14x22 Subsonic Tunnel. The final grid had approximately 29 million nodes.

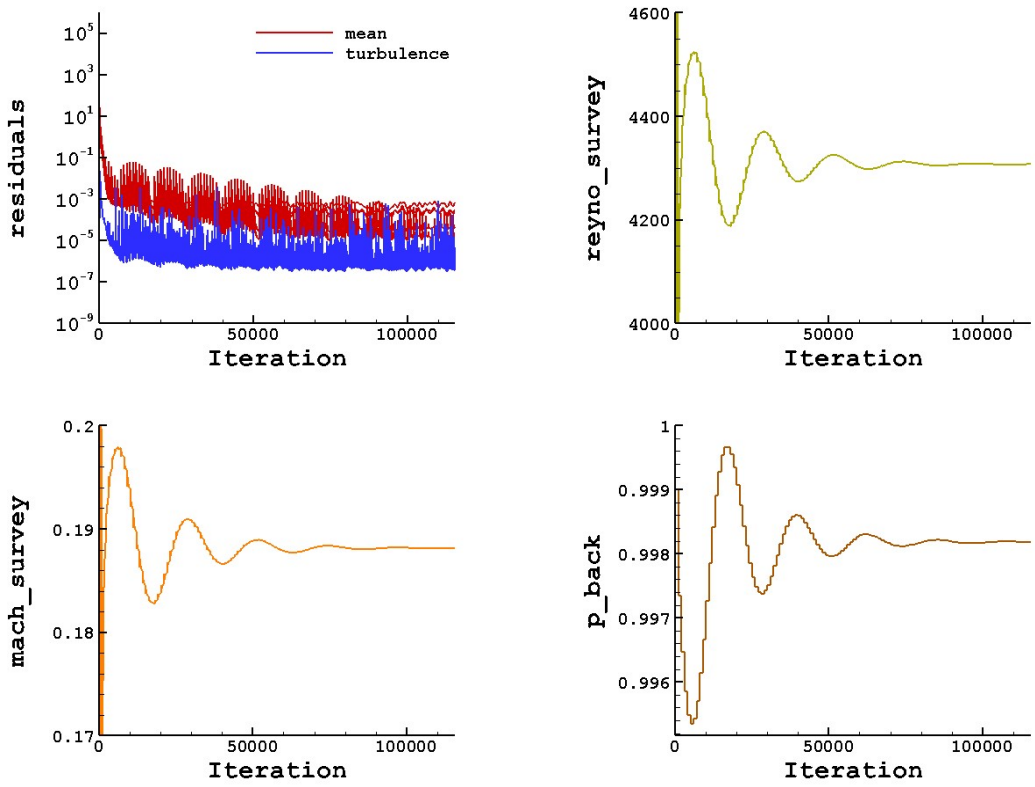

Figure 19. Convergence and PID tunnel controller time history.

Figure 20 shows the comparison of pressure coefficients on the wing. Please note that all wind tunnel static pressure (C_p) data are plotted in the figure and includes measurements taken on both the port and starboard wings and for multiple data collection runs. In general, the results are similar for both the in-tunnel and the free-air simulations and in good agreement with the measurements. The only exception is for the slice at $y = -1663.7$ mm near the wingtip due to the inability of the model to capture the wingtip vortex at coarse mesh resolution. The in-tunnel prediction of C_p is better in capturing the peak at the leading edge of the wing compared to the free-air run. The in-tunnel C_p prediction on the upper surface of the wing is closer to the measurements compared to the free-air runs. Similar differences were also observed in the comparison of in-tunnel vs. free-air simulations using OVERFLOW.[19]

Comparison of the flow separation prediction in the juncture region using free-air and in-tunnel grids is shown in Figure 21. The results of the two simulations in terms of both shape and size are almost identical. The free-air simulation predicted a bubble width of 66.56 mm compared with a width of 66.33 mm in the wind tunnel simulation. The location of flow separation initiation was at 2757.2 mm in the free-air case compared with 2758.1 mm in the wind tunnel simulation. Lee and Pulliam have reported small differences in both the bubble shape and size between the free-air and in-tunnels runs on medium and fine resolution grids using OVERFLOW.[19]

Figure 22 shows the comparison of mean velocities at four different locations. One location is on the fuselage near the leading edge of the wing and three locations are on the wing. The only noticeable (although still relatively small) difference is in the prediction of w component of the velocity for the point on the fuselage. The in-tunnel prediction of the w velocity profile was in better agreement with the experiments for this location. This behavior was also observed in the OVERFLOW simulations.[19] Lee and Pulliam report larger differences for turbulence quantities between the free-air and in-tunnel results in the separation bubble region. The turbulence quantities were not compared in this study because the simulations were on coarse grids. They will be the focus of a future study using higher resolution grids.

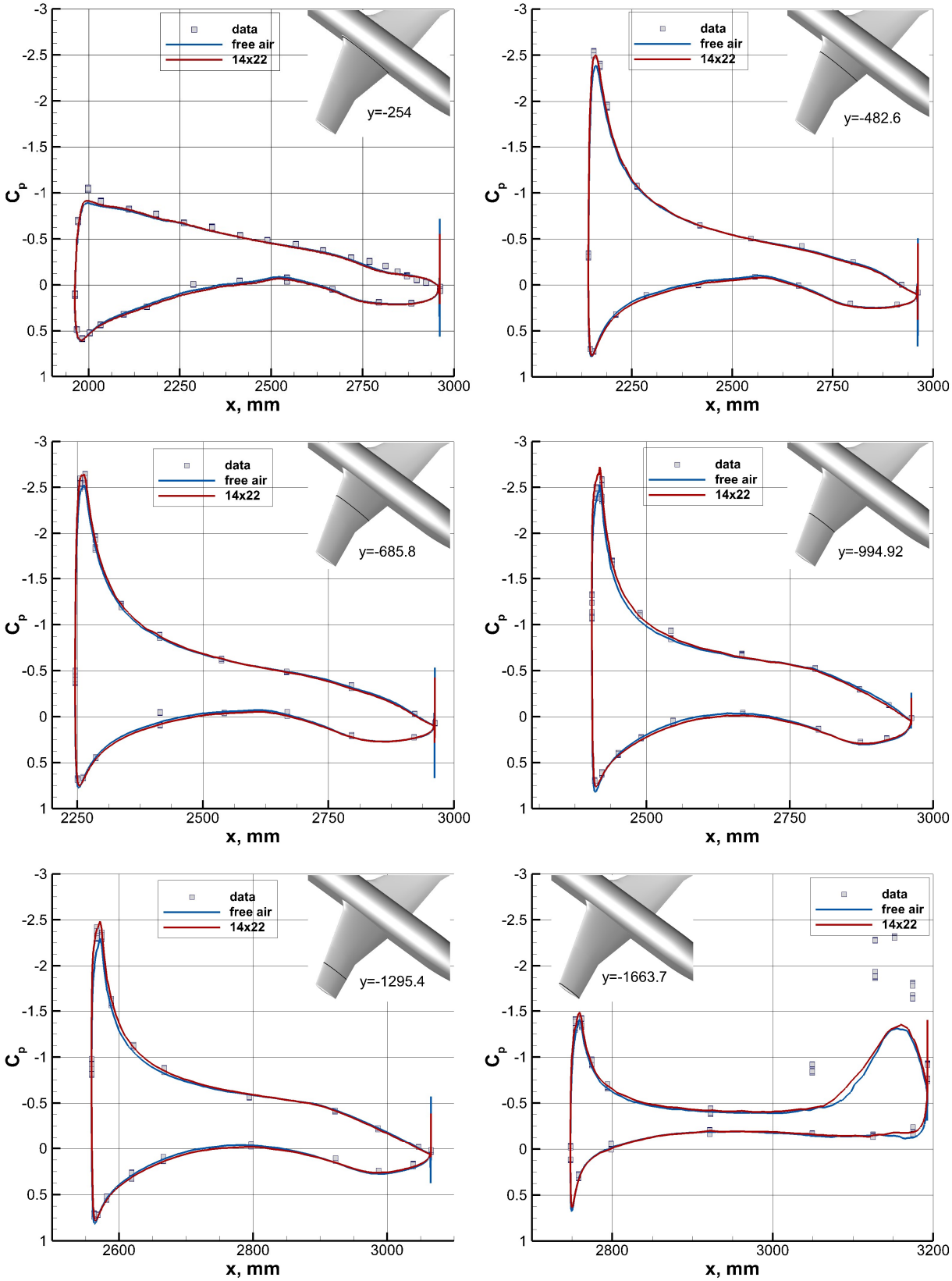

Figure 20. Pressure coefficients on the wing, $\alpha = 5°$. Coarse mesh. Free-air vs. in-tunnel run.

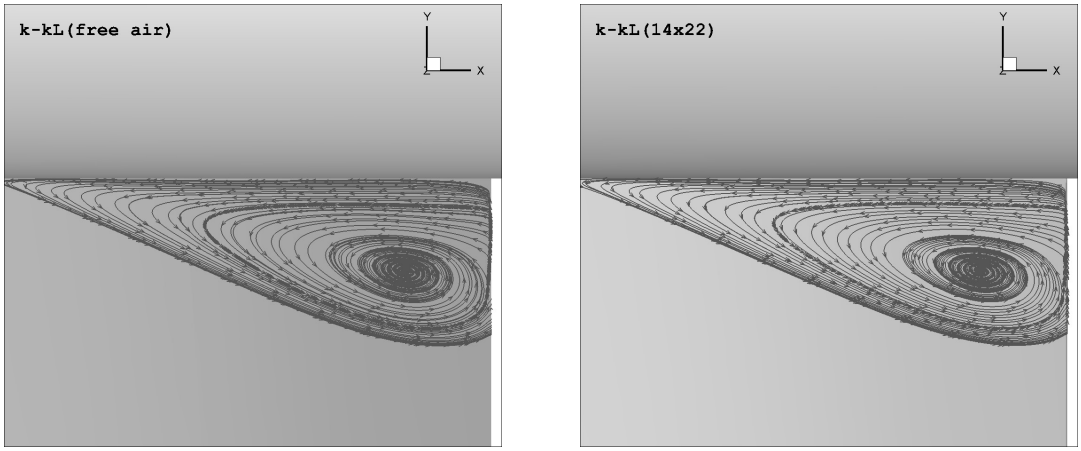

Figure 21. Flow separation in the wing-fuselage juncture region on the coarse grids. Free air result (left) and the in-tunnel result (right), α = 5°, k-kL scheme.

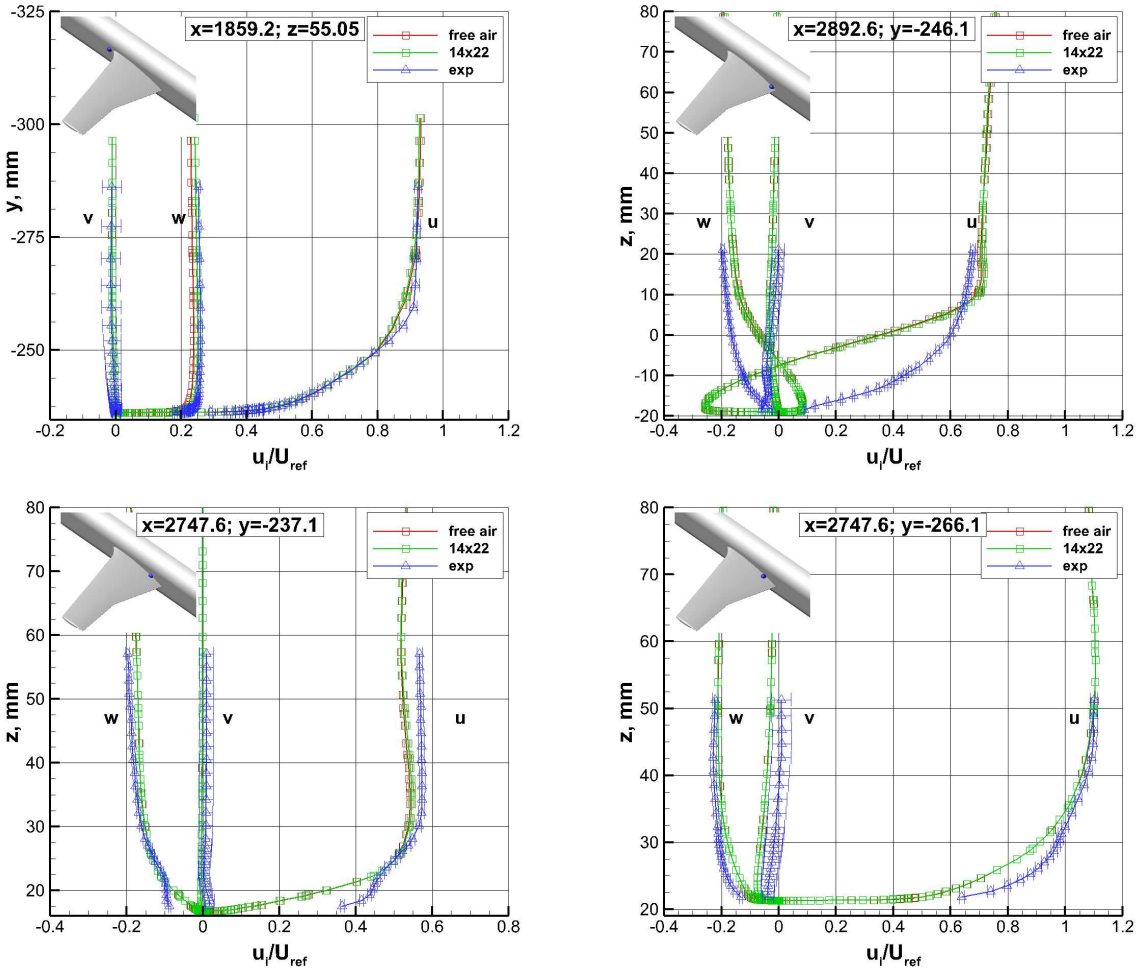

Figure 22. Comparison of mean velocities from the free-air and in-tunnel runs, α = 5°, coarse mesh, k-kL scheme. Results are shown at (*x*, *z*) = (1859.2 mm, 55.05 mm), (*x*, *y*) = (2892.6 mm, –246.1 mm), (*x*, *y*) = (2747.6 mm, –237.1 mm), and (*x*, *y*) = (2747.6 mm, –266.1 mm).

VIII. Summary

The k-kL, k-kL-QCR, k-kL-ARSM, and SA-RC-QCR2000 turbulence models were compared with the Juncture Flow Experiment data for α = –2.5° and α = 5° cases with favorable results. All models were able to predict the mean velocity profiles (on the fuselage and over the wing upstream of the separation bubble) with a reasonably good degree of accuracy. Small deviations in the *u* component of the mean velocity were observed. The surface pressure data also compared well with the measurements. The underestimation in the pressure peak at the wing leading edge seen in the free-air simulations was alleviated in the in-tunnel simulation. In the earlier evaluations of the k-kL family of schemes, the k-kL-ARSM had shown to be the most promising of the three k-kL schemes. In terms of predicting both the bubble size and the flow characteristics in the separation region, the k-kL-ARSM performed better in this evaluation as well.

With the exception of two components of the normal stresses ($u'u'$, $w'w'$), the rest of the turbulence quantities compared well with the measurements for all schemes. This was observed in the locations on the fuselage, on the wing upstream of separation, and inside the separation bubble and for both α = –2.5° and α = 5° conditions.

The k-kL-QCR scheme was compared with the SA-RC-QCR2000 scheme. The computed mean velocities, with the exception of the *u* component, were in good agreement with the measurements for both schemes. In this comparison also, the models had difficulty predicting the $u'u'$ normal stress component. The predictions of $w'w'$ were better at the location closer to the fuselage.

In general, the width of the bubble showed convergence toward the measured width size for all cases while the length was overestimated and the differences in the bubble length at different mesh resolutions were not significant. For the k-kL schemes, the bubble length slightly increased on the fine resolution meshes. The k-kL-ARSM scheme predicted the smallest bubble size compared to other schemes on coarse and medium grids, however, at the fine mesh resolution, the SA-RC-QCR2000 predicted bubble size was approximately the same as the k-kL-ARSM. There were differences in the separation structure for different schemes. The separation flow features predicted by k-kL and k-kL-ARSM were similar, while k-kL-QCR and SA-RC-QCR2000 predicted bubbles shared similar topology. The trends in –2.5° angle of attack case were similar to the 5° angle of attack case. At fine mesh resolution, for α = –2.5°, the SA-RC-QCR2000 scheme predicted the smallest bubble size.

In general, all models predicted early separation (overestimated the bubble length). This can be due to the inability of the models to accurately predict the normal stresses. The discrepancy observed in the prediction of normal stresses was especially large in the case of $u'u'$ near the wall.

Grid resolution-based uncertainty bounds were calculated, which showed that the k-kL-ARSM and k-kL-QCR schemes were least sensitive to changes in mesh resolution and the SA-RC-QCR2000 exhibited the most sensitivity to mesh resolution, especially in the boundary layer. The uncertainty bounds were much smaller compared to the results obtained from a previous[18] on a different family of grid underscoring the importance of mesh clustering in the separation region.

Results of an in-tunnel study using FUN3D's overset and tunnel-controller capabilities were promising. The in-tunnel simulation improved the C_p predictions and small improvement in the *w* component of the mean velocity was also observed. There were no significant differences in the prediction of the separation location, bubble size and bubble shape, between the free-air and the in-tunnel runs. These are preliminary results on a coarse resolution mesh and further work is needed to better quantify the advantages of in-tunnel simulations.

Acknowledgments

This work was supported by the NASA Transformational Tools and Technologies (TTT) Project of the Transformative Aeronautics Concepts Program. The authors would like to thank Chris Rumsey who leads The Juncture Flow Team and the team members: Ponnampalam Balakumar, Judy Hannon, Luther Jenkins, Mike Kegerise, Cathy McGinley, Mujeeb Malik, and Dan Neuhart from NASA Langley; Henry Lee and Tom Pulliam from NASA Ames; Philippe Spalart from Boeing; and Bill Oberkampf. Many thanks to Mike Wiese, Scott Brynildsen, and Norma Farr for providing the grids used in this study.

References

[1]Rumsey, C.L. and Morrison, J.H., "Goals and Status of the NASA Juncture Flow Experiment," NATO Science and Technology Organization, Specialists Meeting on Progress and Challenges in Validation Testing for Computational Fluid Dynamics, AVT-246-RSM-038, Avila, Spain, 26-28 September 2016, Paper Number AVT-246-03.

[2]Rumsey, C.L., Neuhart, D.H., Kegerise, M.A., "The NASA Juncture Flow Experiment: Goals, Progress, and Preliminary Testing (Invited)," AIAA Paper 2016–1557.

[3]Rumsey, C.L., "The NASA Juncture Flow Test as a Model for Effective CFD/Experimental Collaboration," AIAA Paper 2018–3319.

[4]Vassberg, J.C., Tinoco, E.N., Mani, M., Broderson, O.P., Eisefeld, B., Wahls, R.A., Morrison, J.H., Zickuhr, T., Laflin, K.R., Mavriplis, D.J., "Abridged Summary of the Third AIAA Computational Fluid Dynamics Drag Prediction Workshop," *Journal of Aircraft*, Vol. 45, 2008, pp. 781–798.

[5]Levy, D.W., Laflin, K.R., Tinoco, E.N., Vassberg, J.C., Mani, M., Rider, B., Rumsey, C.L., Wahls, R.A., Morrison, J.H., Broderson, O.P., Crippa, S., Mavriplis, D.J., Murayama, M., "Summary of Data from the Fifth Computational Fluid Dynamics Drag Prediction Workshop," *Journal of Aircraft*, Vol. 51, 2014, pp. 1194–1212.

[6]Tinoco, E.N., Broderson, O.P., Keye, S., Laflin, K.R., Feltrop, E., Vassberg, J.C., Mani, M., Rider, B., Wahls, R.A., Morrison, J.H., Hue, D., Gariepy, M., Roy, C.J., Mavriplis, D.J., Murayama, M., "Summary of Data from the Sixth AIAA CFD Drag Prediction Workshop: CRM Cases 2 to 5," AIAA Paper 2017–1208.

[7]Roozeboom, N.H., Lee, H.C., Simurda, L.J., Zilliac, G.G., Pulliam, T. H., "Comparison of Experimental Surface and Flow Field Measurements to Computational Results of the Juncture Flow Model," AIAA Paper 2016-1558.

[8]Kuester, M.S., Borgoltz, A., Davenport, W., "Experimental Visualization of Junction Separation Bubbles at Low- to Moderate-Reynolds Numbers," AIAA Paper 2016–3880.

[9]Kegerise, M.A., Neuhart, D.H., "Wind Tunnel Test of a Risk-Reduction Wing/Fuselage Model to Examine Juncture-Flow Phenomena," National Aeronautics and Space Administration, NASA/TM–2016–219348, 2016.

[10]Lee, H.C., Pulliam, T.H., Neuhart, D.H., Kegerise, M.A., "CFD Analysis in Advance of the NASA Juncture Flow Experiment," AIAA Paper 2017–4127.

[11]Rumsey, C.L., Carlson, J.-R., Hannon, J.A., Jenkins, L.N., Bartram, S.M., Pulliam, T.H., Lee, H.C., "Boundary Condition Study for the Juncture Flow Experiment in the NASA Langley 14x22-Foot Subsonic Wind Tunnel," AIAA Paper 2017–4126.

[12]Lee, H.C., Pulliam, T.H., Rumsey, C.L., Carlson, J.-R., "Simulations of the NASA Langley 14- by 22- Foot Subsonic Tunnel for the Juncture Flow Experiment," NATO Science and Technology Organization, AVT-284 Research Workshop on Advanced Wind Tunnel Boundary Simulation, Torino, Italy, 16-18 April 2018, Paper Number STO-MP-AVT-284-02.

[13]Kegerise, M.A., Neuhart, D.H., "An Experimental Investigation of a Wing-Fuselage Junction Model in the NASA Langley 14- by 22-Foot Subsonic Wind Tunnel," National Aeronautics and Space Administration, NASA/TM–2019–220286, 2019.

[14]Kegerise, M.A., Neuhart, D.H., Hannon, J.A., Rumsey, C.L., "An Experimental Investigation of a Wing-Fuselage Junction Model in the NASA Langley 14- by 22-Foot Subsonic Wind Tunnel," AIAA Paper 2019–0077.

[15]Rumsey, C.L., "NASA Langley Research Center Turbulence Modeling Resource," https://turbmodels.larc.nasa.gov, Accessed: 2019-07-31.

[16]NASA FUN3D CFD CODE, https://fun3d.larc.nasa.gov, Accessed: 2019-07-31.

[17]NASA OVERFLOW CFD CODE, https://overflow.larc.nasa.gov, Accessed: 2019-07-31.

[18]Rumsey, C.L., Carlson, J.-R., Ahmad, N.N., "FUN3D Juncture Flow Computations Compared with Experimental Data," AIAA Paper 2019–0079.

[19]Lee, H.C., Pulliam, T.H., "Overflow Juncture Flow Computations Compared with Experimental Data," AIAA Paper 2019–0080.

[20]Abdol-Hamid, K.S., "Assessments of a Turbulence Model based on Menter's Modification to Rotta's Two-Equation Model," AIAA Paper 2013–0341.

[21]Abdol-Hamid, K.S., "Assessments of *k-kL* Turbulence Model Based on Menter's Modification to Rotta's Two-Equation Model," *International Journal of Aerospace Engineering*, Vol. 2015, 2015, pp. 1–18.

[22]Abdol-Hamid, K.S., Carlson, J.-R., Rumsey, C.L., "Verification and Validation of the k-kL Turbulence Model in FUN3D and CFL3D Codes," AIAA Paper 2016–3941.

[23]Abdol-Hamid, K.S., Carlson, J.-R., Rumsey, C.L., Lee-Rausch, E.M., Park, M.A., "DPW-VI Results Using FUN3D with Focus on k-kL-MEAH2015 (k-kL) Turbulence Model," AIAA Paper 2017-0962.

[24]Abdol-Hamid, K.S., "kL-Based Linear and Nonlinear Two-equation Turbulence Models," *Tenth International Conference on Computational Fluid Dynamics (ICCFD10)*, Barcelona, Spain, July 9-13, 2018, ICCFD10-2018-014.

[25]Abdol-Hamid, K.S., Carlson, J.-R., Rumsey, C.L., Lee-Rausch, E.M., Park, M.A., "Sixth Drag Prediction Workshop Results Using FUN3D with k-kL-MEAH2015 Turbulence Model," *Journal of Aircraft*, Vol. 55, 2018, pp. 1458–1468.

[26]Abdol-Hamid, K.S., "Development and Documentation of kL-Based Linear, Nonlinear, and Full Reynolds Stress Turbulence Models," National Aeronautics and Space Administration, 2018, NASA/TM–2018–219820.

[27]Abdol-Hamid, K.S., "Development of kL-Based Linear, Nonlinear, and Full Reynolds Stress Turbulence Models," AIAA Paper 2019–1878.

[28]Biedron, R.T., Lee-Rausch, E.M., "Rotor Airloads Prediction Using Unstructured Meshes and Loose CFD/CSD Coupling," AIAA Paper 2008–7341.

[29]Carlson, J.-R., "Automated Boundary Conditions for Wind Tunnel Simulations," National Aeronautics and Space Administration, NASA/TM–2018–219812, 2018.

[30]Jenkins, L.N., Yao, C.-S., Bartram, S.M., "Flow-Field Measurements in a Wing-Fuselage Junction Using an Embedded Particle Image Velocimetry System," AIAA Paper 2019–0078.

[31]Gand, F., Deck, S., Brunet, V., Sagaut, P., "Flow dynamics past a simplified wing body junction," *Physics of Fluids*, Vol. 22, 2010, pp. 115111-1–16.

[32]Simpson, R.L., "Junction Flows," *Annual Review of Fluid Mechanics*, Vol. 33, 2001, pp. 415–443.

[33]Biedron, R.T., Carlson, J.-R., Derlaga, J.M., Gnoffo, P.A., Hammond, D.P., Jones, W.T., Kleb, B., Lee-Rausch, E.M., Nielsen, E.J., Park, M.A., Rumsey, C.L., Thomas, J.L., Thompson, K.B., Wood, W.A., "FUN3D Manual: 13.5," National Aeronautics and Space Administration, 2019, NASA/TM–2019–220271.

[34]Anderson, W.K., Bonhaus, D.L., "An Implicit Upwind Algorithm for Computing Turbulent Flows on Unstructured Grids," *Computers and Fluids*, Vol. 23, 1994, pp. 1–22.

[35]Anderson, W.K., Rausch, R.D., Bonhaus, D.L., "Implicit/Multigrid Algorithms for Incompressible Turbulent Flows on Unstructured Grids," *Journal of Computational Physics*, Vol. 128, 1996, pp. 391–408.

[36]Biedron, R.T., Thomas, J.L., "Recent Enhancements to the FUN3D Flow Solver for Moving-Mesh Applications," AIAA Paper 2009–1360.

[37]Spalart, P.R., Allmaras, S.R., "A One-Equation Turbulence Model for Aerodynamic Flows," *Recherche Aerospatiale*, No. 1, 1994, pp. 5-21.

[38]Shur, M.L., Strelets, M.K., Travin, A.K., Spalart, P.R., "Turbulence Modeling in Rotating and Curved Channels: Assessing the Spalart-Shur Correction," *AIAA Journal*, Vol. 38, 2000, pp. 784–792.

[39]Spalart, P.R., "Strategies for turbulence modelling and simulations," *International Journal of Heat and Fluid Flow*, Vol. 21, 2000, pp. 252–263.

[40]Rotta, J.C., "Statistische Theorie nichthomogener Turbulenz," *Zeitschrift für Physik*, Vol. 129, 1951, pp 547–572.

[41]Menter, F.R., Egorov, Y., "The Scale-Adaptive Simulation Method for Unsteady Turbulent Flow Predictions. Part 1: Theory and Model Description," *Flow, Turbulence and Combustion*, Vol. 85, 2010, pp. 113–138.

[42]Egorov, Y., Menter, F.R., Lechner, R., Cokljat, D., "The Scale-Adaptive Simulation Method for Unsteady Turbulent Flow Predictions. Part 2: Application to Complex Flows," *Flow, Turbulence and Combustion*, Vol. 85, 2010, pp. 139–165.

[43]Rumsey, C.L., Gatski, T.B., "Summary of EASM Turbulence Models in CFL3D with Validation Cases," National Aeronautics and Space Administration, 2003, NASA/TM–2003–212431.

[44]Speziale, C.G., Sarkar, S., Gatski, T.B., "Modeling the pressure-strain correlation of turbulence: an invariant dynamical systems approach," *Journal of Fluid Mechanics*, Vol. 227, 1991, pp. 245–272.

[45]Roe, P.L., "Approximate Riemann Solvers, Parameter Vectors, and Difference Schemes," *Journal of Computational Physics*, Vol. 43, 1981, pp.357–372.

[46]Celik, I.B., Ghia, U., Roache, P.J., Freitas, C.J., Coleman, H., Raad, P.E., "Procedure for Estimation and Reporting of Uncertainty Due to Discretization in CFD Applications," *Journal of Fluids Engineering*, Vol. 130, 2008, 078001.

[47]Noack, R.W., "SUGGAR: A General Capability for Moving Body Overset Grid Assembly," AIAA Paper 2005–5117.

[48]Noack, R.W., "DiRTlib: A Library to Add an Overset Capability to Your Flow Solver," AIAA Paper 2016–1557.